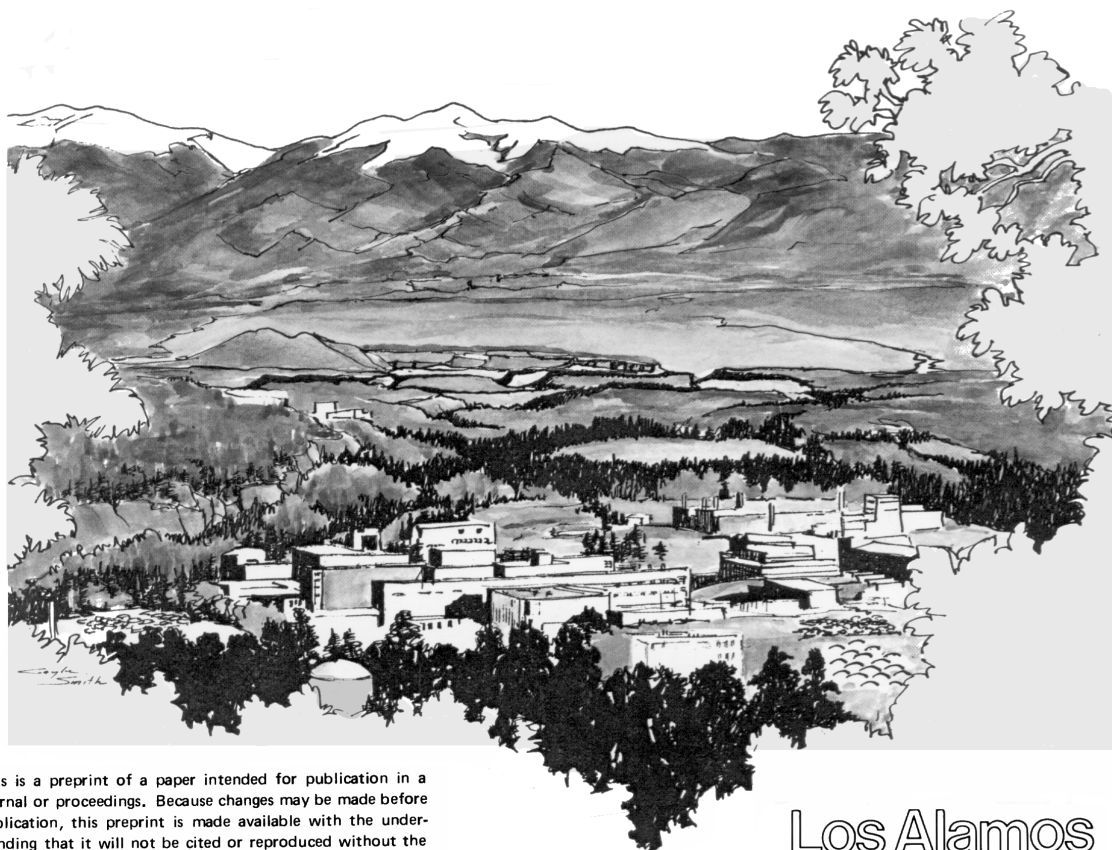**TITLE:** Eruptive Mechanisms of the Neapolitan Yellow Tuff
Interpreted from Stratigraphic, Chemical, and
Granulometric Data

AUTHORS: Kenneth Wohletz[1], Giovanni Orsi[2],
and Sandro de Vita[2]

[1]*Los Alamos National Laboratory, Earth and Environmental Sciences Division, Los Alamos, NM 87545*
[2]*University of Naples Federico II, Department of Geophysics and Volcanology, Naples, Italy 80138*

Los Alamos
Los Alamos National Laboratory
Los Alamos, New Mexico 87545

ERUPTIVE MECHANISMS OF THE NEAPOLITAN YELLOW TUFF INTERPRETED FROM STRATIGRAPHIC, CHEMICAL, AND GRANULOMETRIC DATA

by

K. Wohletz[1], G. Orsi[2], and S. de Vita[2]

[1]*Earth and Environmental Sciences, Los Alamos National Lab, Los Alamos, NM 87545 USA*
[2]*Dipartimento di Geofisica e Vulcanologia, Università di Napoli, 80138 Napoli, Italy*

ABSTRACT

The Neapolitan Yellow Tuff (12 ka) is the second largest pyroclastic deposit of the Campanian Volcanic Area covering at least 1000 km^2 with conservative estimates of volume placed at 40 km^3. Previous studies showed that this mainly trachytic deposit, composed of two members, was erupted by (1) a central vent, mostly phreatoplinian phase (Lower Member) that generated pyroclastic surges and fallout reaching 34 km from the vent followed by (2) a multiple vent, phreatomagmatic and magmatic phase (Upper Member) associated with onset of caldera collapse that produced surges extending 14 km from the vent. The Lower Member is well bedded and comprises 13 subunits that alternate between phreatoplinian surges/flows and Plinian pumice-and-ash fallout. The Upper Member is relatively lithic-rich and more massive in character. For both members, magma compositions vary from alkali trachyte through trachyte to latite, which does not fit a simple inversion of magma chamber gradients. Calculations based on magma chemistry show an increase in magma density, a decrease followed by an increase in viscosity, and a general decrease of gas fraction during the course of both eruptive phases. After migrating to a depth of about 400 m, calculated fragmentation depths gradually rise during each phase. Application of sequential fragmentation/transport analysis to granulometric data shows for the lower member an average ratio of phreatomagmatic to magmatic components of 70:30 while the upper member shows an average ratio of 80:20. However, considering the tephra volume represented by samples, computed water/magma interaction ratios (R) are shown to fluctuate but generally decrease from about 0.65 to 0.05 during eruption of the Lower Member while the Upper Member shows R fairly constant at about 0.1. Furthermore, surge/flow runout distances and estimates of eruptive velocities from R values show that column collapse heights were extremely high (6 to 7 km) during the first phase and were substantially lower during the second phase (2 to 3 km). Vent radii required for calculated eruption velocities of 180 to 370 m/s are between 70 and 300 m, suggesting a cumulative eruption duration of over 10 hours, perhaps spanning one to several days.

INTRODUCTION

The Neapolitan Yellow Tuff (NYT) is the second largest pyroclastic deposit of the Campanian Volcanic Area. Conservative estimates of the area covered and volume of the NYT are 1000 km^2 and >40 km^3, respectively. While the deposit is generally gray and poorly indurated in distal areas, it is yellow and zeolitized in the proximal Neapolitan-Phlegraean area. It was first recognized in the urban Neapolitan area, hence its name. Many other tuffs in the Neapolitan-Phlegraean area are also yellow and zeolitized and have been considered part of the NYT, but Orsi et al. (1991; 1992) have recognized that most of these tuffs postdate the NYT and come from other source vents.

The NYT has attracted the interest of geologists for almost two centuries (*e.g.*, Breislak, 1801). De Lorenzo (1904) was the first scientist to propose a comprehensive hypothesis on the evolution of the Phlegraean Fields, subdividing it into three periods the second of which was dominated by the eruption of the NYT. In 1950 many authors described the geology of the Neapolitan area and concluded that there were various yellow tuffs, erupted by different vents at different times. In particular, Rittmann (1950) suggested that the tuffs were emplaced by nuées ardentes at high speed and high temperature. The existence of different, but texturally similar tuffs, was also supported by Rosi et al. (1983), Capaldi et al. (1987), and Rosi and Sbrana (1987). This division of the yellow tuffs was also suggested in recent times (Scherillo and Franco, 1967; Lirer and Munno, 1975; Di Girolamo et al., 1984). Orsi and Scarpati (1989) first recognized the NYT up to the foot of the Apennine Mountains, north of the town of Caserta, and proposed a reconstruction of its eruptive history.

The NYT eruption took place inside the Phlegraean caldera that collapsed after the eruption of the ~34 ka b.p. Campanian Ignimbrite (Alessio et al., 1971, 1973, 1974; Cita et al., 1977; Barberi et al., 1978, 1991;Cassignol and Gillot, 1982; Rosi et al., 1983; Rosi and Sbrana, 1987; Deino et al., 1992). The 12 ka age of the NYT is based mostly on ^{14}C age determinations on paleosols underlying the tuff (Alessio et al., 1971; Lucini and Tongiorgi, 1959; Cassignol and Gillot, 1982; Rosi and Sbrana, 1987).

Orsi et al. (1991; 1992) in their extensive study of the NYT have proposed a more detailed, hypothetical reconstruction of the NYT eruption and magma system based on the relationships between eruptive dynamics and magma chamber withdrawal, and the timing of caldera collapse, all of which are constrained by field evidence, stratigraphic, granulometric, and compositional data. These authors have shown that the compositional gradients of the NYT sequence, comprising texturally distinct lower and upper members, cannot be interpreted as the

inversion of a compositionally zoned magma body with magma becoming less evolved during the course of the eruption. Changes in composition perfectly match changes in eruption dynamics. Orsi et al. (1991) have presented a detailed reconstruction of the magmatic system feeding the NYT eruption and of low-pressure differentiation processes.

Scarpati et al. (1993) and Cole and Scarpati (1993) have also recently recognized the two main members of the NYT described by Orsi et al. (1991), addressing stratigraphic, granulometric/morphometric, and petrochemical variations, which they interpret with respect to eruptive phases and emplacement mechanisms. However, we take field observations and laboratory data further in quantitative interpretation than do previous authors. It is the goal of this paper to extend the interpretation of the remarkable data set collected by Orsi et al. (1991) and reproduced by Scarpati et al. (1991). In the following pages we summarize stratigraphic and petrological data and then proceed with an attempt at modeling this information to gain quantitative physical volcanological insight. Readers are encouraged to compare our results with those of previous studies.

STRATIGRAPHY AND PETROLOGY

The NYT sequence is divided into two members named Lower Member (LM) and Upper Member (UM) (Figs. 1a, 1b). They are distinguishable on the basis of textural characteristics, dispersal, and magma composition. The products of the NYT comprise aphryric or sub-aphyric latites to alkali trachytes with phenocrysts (<3% by volume), often forming glomeroporphyritic textures. Phenocrysts in order of decreasing abundance are sanidine, plagioclase, clinopyroxene, biotite, magnetite, and rare apatite. Xenocrysts of sanidine in latite, anorthitic plagioclase in trachyte and alkali trachyte, reversely zoned plagioclase, and two clinopyroxenes are evidence of mineralogical disequilibrium.

Stratigraphy and Dispersal

The boundary between the two members is usually well defined by a sharp variation in textural characteristics (from fine ash-rich beds containing accretionary lapilli to coarse ash-rich beds) and/or disconformity. No evidence of soil development between the two members has been found. LM displays distinct textural and dispersal characteristics of interlayered phreatoplinian and magmatic tephra. It is the largest trachytic phreatoplinian eruption reported to date (*e.g.*, Self and Sparks, 1978; Self, 1983; Walker, 1981; Branney, 1991). It reaches a

distance of 34 km from the eruptive vent (Fig. 1a), and its thickness varies from 11 m in the most proximal exposures inside the Phlegraean caldera in the Quarto Plain, to 2.3 m in the intermediate area of San Severino outside the caldera depression, to 0.85 m at Sant' Angelo in Formis, at the foot of the Apennine mountains. Based on these measurements, LM's aspect ratio (Walker, 1983) is about 2 x 10^{-4}. In contrast, UM has been found at a maximum distance of only ~14 km from the supposed eruptive vent (Fig. 1a). Its dispersal and textural character is phreatomagmatic, while its thickness varies from about 100 m in the Quarto Plain, to 7 m at Scarafea in the Caserta Plain (aspect ratio ≈2 x 10^{-3}).

Lower Member (LM). LM includes 13 layers of variable thickness, designated LM1 through LM13 from base upward. Its textural and sedimentological characteristics change with distance from the vent (Fig. 1b). Therefore a LM Proximal (LMP) and a LM Distal (LMD) facies can be recognized at distances <9 km and > 9 km from the supposed vent area, respectively. At around 9 km layers of both facies intercalate constituting an intermediate facies (LMI). The LMP facies mostly comprises surge layers with subordinate pumice-and-ash fallout while the LMD facies is dominated by ash and pumice-and-ash fallout layers with subordinate surge beds. The two facies include a common basal layer (LM-1) that does not change significantly in textural and depositional characteristics over the entire outcrop area. The LM Proximal facies is composed of the basal LM-1 and a complex sequence dominated by surge beds. Its thickness varies from 11 m at Quarto to 4.5 m at Zaccaria. The stratigraphic sequence of the LMP facies varies widely due to the localized distribution of the single beds. The succession exposed at Quarto most completely represents the depositional sequence. The LMI facies is composed either of layers of LMD and LMP facies or of layers resulting from the interfingering of the two deposits. The LMI facies beds are usually very thin and represent distal deposits of surge clouds, typified as the depositional sequence at Scarafea. The LM Distal facies is mainly composed of ash fallout beds with 6 intercalated pumice-and-ash fallout layers, typified by the deposits cropping out at Sant' Angelo in Formis. Poor sorting in some layers suggests possible surge involvement at this distal exposure. In intermediate and distal areas, pumice-and-ash-fallout layers are markers for stratigraphic reconstruction and correlation of the sequence (Fig. 1b). In proximal areas, all of these beds, except LM-3, are missing. Therefore, correlation of the proximal ash fallout layers with their distal counterparts in some cases is speculative. A detailed description of the LM is given in Appendix A.

Upper Member (UM). UM is composed of pyroclastic flow and surge deposits. The sequences exposed in sections either at varying distances from the supposed vent or at different azimuths around the caldera show considerable variation. Pyroclastic flow deposits dominate in exposures inside the Phlegraean caldera, while pyroclastic surge beds comprise most sections outside of the

caldera depression. The textural variability with azimuthal position is evidence that UM was generated by multiple ring-fracture vent eruptions and that there was likely flow transformation (Fisher, 1983) during runout of UM across the Phlegraean caldera scarp. Although we do not find distinct stratigraphic markers that can be confidently correlated, we have designated 7 intervals for the samples described in this paper.

We recognize proximal and distal facies in UM. The proximal facies of UM is exemplified by the stratigraphic section at Quarto. At this location, while LM drapes over the Phlegraean caldera wall, basal UM beds up to 0.45 m thick show unconformable onlapping of surge units onto LM. Above this unconformity, going upwards, we see a thin (0.7 m) pyroclastic flow bed, 1.5 m of coarse and fine pumice and ash beds, and a sequence of 3 massive pyroclastic flow layers, the thinnest of which is 2.4 m and the thickest is 4.0 m, topped by thin (7 to 35 cm) ash-cloud surge units, and finally 1.2 m of surge beds topped by a soil horizon. The best exposures of the distal UM are found at Scarafea. The basal contact with LM is conformable, and the upward sequence is dominated by 5 pyroclastic surge units, the thinnest of which is 0.4 m thick and the thickest is 2.8 m thick. These surge units are separated by fine ash beds and in places by erosive intervals.

Petrology

The NYT rocks range in composition from latite to alkali trachyte. Compositional variations of pumice fragments within the stratigraphic section allow a fourfold distinction of the sequence that, from the base upward, is divided in LM alkali trachyte (LMat), LM trachyte (LMt), UM alkali trachyte (UMat) and UM trachyte-to-latite (UMt) (Fig. 2a). Glass shards from the trachytic pumice-and-ash fallout beds of LM, show all the chemical compositions displayed by the pumice fragments. The two trachytic groups are distinguished on the basis of trace element, K_2O, Na_2O, SiO_2 and P_2O_5 contents, whereas the two alkali trachytic groups are distinguished by their stratigraphic position. Appendix B summarizes the magma chamber model of Orsi et al. (1992) for the NYT eruptions.

Conservative dense rock equivalent (DRE) estimates of the erupted volumes of LMat, LMt, UMat, and UMt are 3 km^3, 7 km^3, 20 km^3, and 10 km^3, respectively. Temperature estimates, based on the ternary feldspar geothermometer (Fuhrman and Lindsley, 1988), give values of 786±40°C, 788±40°C and 798±40°C at 1 kbar for the alkali trachyte, trachyte, and latite magmas, respectively. We do not have estimates of the pre-eruptive magmatic water content of the NYT. (Orsi et al., 1991) show a positive correlation between loss on ignition

(LOI) weights with differentiation index and Zr abundance displayed by the pumice, which suggests that water behaved as an incompatible element (Wolff et al., 1990) and a volatile gradient likely existed in the chamber.

As discussed above, the NYT tephra consist of pumice and ash fragments. Whereas the ash components show a range of compositions within individual beds, pumices are compositionally uniform within individual beds. Because the ash samples may include effects of syneruptive commingling, we focus this study on averaged pumice analyses that represent LM layers 1, 2, 3, 5, 9, 11, 13 (Table 1) and 7 intervals within UM, going upward through UM alkali trachytes to UM trachytes (Table 2). Some discussion of ash compositions noted sheds light on the nature of syneruptive fragmentation mechanisms and commingling of magmas within the conduit. Scanning electron microscopic observations demonstrate that the ash matrix comprises vesicular and nonvesicular (blocky) shards. X-ray energy dispersive spectral analyses of these shards (Table 3) show that these two shard types have distinct compositions for LM-3 and LM-4 (a fallout and surge layer respectively), the vesicular shards showing latitic compositions, and the blocky shards showing alkali trachytic affinities. These compositions are in general accordance with x-ray wavelength analyses reported by Orsi et al. (1991; 1992). Furthermore, these authors have explained why these shard compositions are found in tephra dominated by trachytic pumice compositions by showing that magma withdrawal simultaneously tapped all three magma layers in the chamber during eruption of these units. In the magma chamber model (Appendix B), the alkali trachyte magma resides in the top portion of the chamber. Recognition of the blocky shard texture suggests that only the alkali trachyte magma experienced efficient water/magma interaction, while the trachytic and latitic magmas were withdrawn from greater depths and did not encounter external water during their journey through the vent conduit. This observation strengthens the model presented by Orsi et al. (1992) regarding the magma withdrawal dynamics of the NYT eruptions.

MODELING OF CHEMICAL DATA

The relationships between magma chemistry and documented variations in dispersal, stratigraphic textures, and tephra characteristics of the NYT suggest that magma chemistry is one important controlling parameter of the eruption dynamics. In exploring this hypothesis, we model conceivable variations in magma density, viscosity, and volatile content as a function of stratigraphic position of analyzed samples.

Because the NYT has a very low crystal content, we have not been able to make quantitative measurements of crystal glass inclusions that allow assessment of the magma volatile content. The analyzed pumices are all fresh and have similar phenocryst content, and for these trachytic compositions, volatile abundance represented by LOI values should be very close to actual glass water content. Dunbar et al. (1989) showed a positive correlation of glass inclusion water contents to Cl abundances in glasses from Taupo magmas. In Figure 3, we show a similar correlation of Cl with LOI values for the NYT samples analyzed. If seawater ($Cl \approx 2.0$ wt%, $S \approx 0.08$ wt%) had significantly contributed to Cl and LOI values, then S abundance should also show a marked positive correlation with LOI, but in fact it generally decreases with LOI (Fig. 3). Furthermore, the aforementioned correlation of LOI with differentiation index and Zr abundance further indicates that LOI values reflect relative changes in magma volatile content. These considerations support making a first-order assumption that LOI values in some way reflect primary magmatic water contents. Further discussion of this perhaps controversial assumption is included in Appendix C.

The major element chemical data were analyzed using an adaptation of previous methods (Bottinga and Weill, 1970; Lange and Carmichael, 1987) for estimating bulk densities from partial molar volumes of the oxides. Viscosity estimation was achieved by combining modifications of Shaw's (1972) and Bottinga and Weill's (1972) algorithms to take into account pressure effects on viscosity (*e.g.* Kushiro, 1986). These methods (Appendix D) were adapted to computer solution, such that results obtained are fully uniform.

In application of the methods, described in Appendix D, some interesting trends in magma compositional variation can be correlated to stratigraphic position, which allow further interpretation of eruption dynamics. The results in Figures 4 through 9 show variations in estimated magma density, viscosity, and vesicularity as a function of gas content and pressure.

Because the samples contain a significant volatile fraction, assumed to be H_2O, pressure has an important effect on the solubility while temperature has a relatively smaller effect (McMillan and Holloway, 1987). Where H_2O content is greater than solubility limits, vesicles develop in the magma greatly decreasing the bulk density. Figure 4a and 4b show bulk densities of samples at a pressure at which all H_2O is still in solution. The three magma types have distinct ranges in density with alkali trachyte the least dense and latite the most. In Figure 4a, density is shown to markedly increase throughout the eruption of both the lower and upper members; the division between the two members is marked by a rapid drop in density. Note that this density increase reflects the variation of magma chemistry erupted with time; however, the density increase is significant with respect to dispersal of erupted products, which will be

discussed later. For all samples density was calculated as a function of pressure. The pressure at which all H_2O is in solution marks a level in the magma chamber above which exsolution begins. In Figure 4b, we find that this vesiculation pressure increases with degree of chemical evolution, latites showing lowest pressure (<300 bars), the trachytes having intermediate pressures (400 to 900 bars), and the water initially exsolving from alkali trachytes between 900 and 1400 bars.

Orsi et al. (1991) show that CaO abundance in the NYT magmas is a good proxy for differentiation index. In Figure 5 we have plotted the pressure at the vesiculation depth versus CaO, which shows a general decrease of pressure with increasing CaO (decreasing differentiation). Still there is apparent fluctuation of pressure around this general decrease for the alkali trachytes and trachytes suggesting that volatile contents do not systematically vary with differentiation.

From inspection of Figures 4 and 5, the physical parameters of density and pressure at the exsolution surface are related to compositional variations and not necessarily to the three identified magma layers. Because the alkali trachytes and trachytes have roughly homogenous composition, the physical properties can be correlated to the magma layer from which they were erupted. But the third magma type, which varies in composition from alkali trachyte to latite, is not distinguished by its physical properties, which cover a wider range than either of the other two magma types.

Figure 6 shows plots of estimated maximum and minimum viscosities for samples studied. Maximum magma viscosities are those found at 1 bar pressure, using the method of Shaw (1972) corrected for suspension effects of crystals and vesicles. The minimum values are found at a high pressure where water is completely dissolved in the magma, using the method of Bottinga and Weill (1972) without suspension effects. At that pressure both viscosity methods predict similar values. In Figure 6a, we show maximum and minimum viscosity variation with stratigraphic position. Both viscosities show an overall decrease during the course of eruption of both members, followed by an increase at the end of each member for minimum viscosities. Figure 6b shows viscosity variations as a function of magma density. In this plot, alkali trachytes show both the highest viscosity values and greatest fluctuation with density, the trachytes show lowest viscosities, and latites intermediate values of viscosity. Furthermore, a plot of viscosity as a function of pressure at exsolution (Fig. 6c) shows a general decrease in viscosity with increasing pressure for both the trachytes and alkali trachytes. The bearing on eruption mechanisms these viscosity and density variations is discussed below.

Papale and Dobran (1992) and Dobran (1992) have demonstrated the importance of magma viscosity in determining the nature of magma ascent in the conduit during explosive eruptions. With increasing magma viscosity, mass flux in the conduit below the fragmentation surface decreases because of the retarding effects of viscous forces. Considering movement of magma at a constant speed below the fragmentation surface in a conduit of constant width, the ratio of magma density to viscosity determines the Reynolds number. Spera (1984) showed the Reynolds number to be the dominant factor in determining the nature of magma withdrawal during eruption. Where viscous forces are large, there is less likelihood of commingling of magmas from different layers in the magma chamber during eruption. To show how this parameter might have changed during the course of the NYT eruptions, we illustrate in Figure 6d a plot of density/viscosity *vs* stratigraphic position. This parameter first increases to a point midway in the course of each member's eruption after which it declines. This change suggests that intermediate stages of each member's eruption should show the greatest effects of syneruptive magma mixing with the effect most prominent in LM products.

In addition to magma density and viscosity variations during the NYT eruptions, there are marked changes in *apparent* volatile abundances as well, assuming the significance of LOI values discussed above for which errors on average values are ±0.15 wt%. Figure 7a is a plot of gas volume fraction at atmospheric pressure with stratigraphy for LM and UM. With high gas contents interpreted at the beginning of each member, LM shows a gradual decline of gas fraction while UM shows steady values throughout the eruption but with a rapid decrease during its final eruptions. These trends reflect the minor variation in erupted magma composition for LM but extreme compositional changes during UM eruptions. In Figure 7b gas fractions, calculated as a function of depth, are plotted *vs* the Shaw (1972) minimum and maximum viscosities (with and without suspension effects, respectively). Minimum viscosities demonstrate a marked increase above a hypothetical fragmentation level (gas fraction = 0.75) where melt polymerization is increased by the rapid decrease in dissolved volatiles. Maximum viscosities show both melt polymerization and suspension effects where vesicle growth and water dissolution continuously evolve with gas fraction. Because the lower viscosity values are those calculated to characterize the NYT magmas while at high pressure in the magma chamber, vesicle growth should be a function of the depth in the chamber from which the NYT tephra were erupted (*i.e.*, tephra erupted from the top of the chamber should show smaller bubble sizes than those erupted from great depths). We are presently making vesicle size measurements to test this hypothesis.

Noting the continuous exsolution of volatiles from the magma during magma withdrawal, plots of gas fraction *vs* pressure are useful in showing the evolution of NYT products within the

magma chamber before their eruption. In Figure 8a, curves display the exponential rise in gas fraction from high (deep) to low (shallow) pressure (locations) in the magma chamber for each sample. The exsolution surface can be described at a pressure where gas fraction curves reach very small (0.001) values. One can view this plot as a representation of the magma chamber where depth is shown by pressure and the evolution of vesicles follows the curves upward to lower pressures eventually reaching the fragmentation surface in the conduit where gas fraction is about 0.75. This plot illustrates the large change of gas fraction at high pressures that become very small as the magma reaches the fragmentation surface. In Figure 8b, the fragmentation surface is shown in an expanded view, and one can see a wide range of pressures over which this fragmentation surface could have fluctuated during eruption of successive products. In both Figures 8a and 8b we see that the alkali trachyte begins exsolution (> 900 bars) and fragmentation (> 90 bars) at greater pressures than the trachyte (>400 and > 50 bars, respectively) and latite magmas (<400 and <50 bars, respectively).

The depth of the exsolution and fragmentation surfaces can be estimated by assuming lithostatic pressure gradients and volatile abundances from averaged LOI values. The depth of the exsolution surface occurs at pressures where the magma first becomes supersaturated, while that of the fragmentation surface is the pressure at which the gas fraction (vesicle volume fraction) reaches ~0.75. Dobran (1992) shows that pressure decreases from approximately lithostatic to a much lower gas-dynamic value over an interval of several meters above the fragmentation surface in the conduit. For simplicity we calculate the depth of the fragmentation surface where pressure has not yet decayed from lithostatic. Using an average overburden density of 2.35 Mg/m^3 to find depth (appropriate for crustal rocks of this area), Figure 9 shows the fluctuation of fragmentation and exsolution depths during the course of eruption of LM and UM. Both curves show sympathetic variation because they are calculated solely as a function of volatile content. In actuality, these depths are also controlled by gas diffusive rates, vesicle growth kinetics, and magma flow regime, which no doubt would complicate this picture. In LM, the fragmentation surface initially is at a depth of about 450 m and rises to less than 400 m where its remains relatively steady until the last part of the eruption where it rises to a depth of about 250 m. For UM the fragmentation surface reaches deeper levels in the conduit (~600 m) before rising to <250 m depth near the end of the eruption. However, each member shows three general trends in fragmentation surface depth: an early rise, a middle time plateau, and a final rise again.

MODELING OF GRANULOMETRIC DATA

Granulometry provides a complex but nonetheless informative data set that holds information about mechanisms of tephra formation and dispersal. The general grain-size characteristics of NYT samples are described by Orsi et al. (1991). In this study, we first demonstrate distinct variations in granulometric data for samples taken from different stratigraphic positions that can be related to progressive changes in eruptive dynamics already established by field observation and chemical modeling. Then these data are further analyzed to provide a systematic basis for interpretation of stratigraphic variations with regard to fragmentation mechanism (magmatic or phreatomagmatic) and modes of transport in pyroclastic surges and flows. Appendix E describes the granulometric modeling technique

The analysis included 90 samples that are representative of most layers of LM and of beds of UM collected at variable distance from the vent. We found sample distributions to be strongly polymodal. Microscopic observation revealed the polymodality to be 5 distinct subpopulations consisting of crystals, pumice, shards (equant and vesicular), and lithic fragments, all of distinct densities and shapes. These 5 subpopulations were found in all samples in varying degrees of prominence. Once the modes for these subpopulations were identified in a bulk sample comprising a weighted average of all samples, it was a simple task to distinguish the subpopulations in individual samples.

As a general characterization of sample data, a sorting (σ_ϕ) *vs* median diameter (Md_ϕ) diagram (Walker, 1971) is shown in Figure 10a. LM samples show distinct characteristics of fallout and flow, while UM samples are within the flow field and overlap with the surge field (see Wohletz, 1983). We identify those fine-grained samples of both members as being distinctly phreatomagmatic (PhM) shown within a field enclosed by a bold line, which correspond to hydrovolcanic grain-size characteristics described by Sheridan and Wohletz (1983). These results have supported the field identification of sample bedding textures. One can see from this plot that there is a strong PhM contribution in NYT tephra. As observed in the field, LM shows alternations between fallout and flow/surge layers, while UM is more texturally homogeneous. These relationships are displayed by a plot of Md_ϕ and σ_ϕ *vs* stratigraphy (Fig. 10b) in which these parameters show opposite trends in LM but not in UM.

Fragmentation

The abundance of the five observed subpopulations are shown in Figure 11 as subpopulation fraction *vs* subpopulation mode (ϕ_m). Best-fit polynomial curves for LM and UM data define two groupings of subpopulations: coarser modes 1 and 2 can be separated from those of fine subpopulations 3, 4, and 5 by a line drawn at -0.67 ϕ. At this point, it is convenient to assign these groupings to magmatic and phreatomagmatic origins, but we will later develop this hypothesis and support it with different methods. With this concept, these data support field observations that LM is composed of interlayered magmatic and phreatoplinian products as also born out by Figure 10b. In contrast, UM is much more homogenous in field appearance without distinct separations of these two tephra types, but Figure 10a does show a predominance of PhM components.

Because subpopulation dispersion (or sorting, γ) is very sensitive to fragmentation mechanism, we further explore the possibility that subpopulations can be distinguished by their mode in Figure 12 in which a fragmentation factor is plotted *vs* mode. The fragmentation factor chosen (expressed as ϕ_m/γ) discriminates the relative contribution of magmatic and phreatomagmatic fragmentation mechanisms in development of the size distribution of each sample. This figure shows that the variation in these parameters is very uniform except at the extreme coarse and fine tails. Despite sample disaggregation, the data scatter in this plot indicates particle aggregation caused by accretionary lapilli or zeolitization has resulted in anomalous dispersion values. By separating the data at 0 phi, we find that coarse modes have values of the fragmentation factor greater than 0 while fine modes have negative values. This discrimination separates magmatic from phreatomagmatic subpopulations and is supported by field, laboratory, and theoretical observations described by Sheridan and Wohletz (1983) and Wohletz (1983), which show that magmatic tephra have coarser grain sizes and poorer sorting (more negative γ values) than do phreatomagmatic tephra. In Figure 13, the distinct character of the fragmentation factor is shown as a histogram of average values for each of the 5 subpopulations, allowing us to interpret subpopulations 1 and 2 as being dominantly formed by magmatic fragmentation and subpopulations 3, 4, and 5 formed by phreatomagmatic fragmentation.

With the preceding arguments for distinguishing magmatic and phreatomagmatic components of the studied samples, we further wish to represent the relative contribution of these components in LM and UM (Figure 14). Overall, both members show a strong phreatomagmatic character, but magmatic tephra are more distinct in LM ($\approx$30 wt%, 25 wt% when normalized to stratigraphic thickness) than in UM ($\approx$20 wt%). In order to find how the water/magma mass ratio

(R) varied during the course of the NYT eruptions, we attempt to find a representative R value for each stratigraphic interval. Assuming that the fraction of phreatomagmatic constituents is a measure of water abundance and that magmatic constituents are a measure of magma abundance during each eruptive phase, we normalize their ratio to 1 (where all fragmentation is phreatomagmatic) to give an estimate of R for each sample. However, the tephra deposits become finer grained with transport distance, because fine fractions are eleutriated during transport of pyroclastic surges and flows and have slower terminal velocities during fallout. This consideration requires an analysis of variation of calculated R values with distance. Figure 15 shows the gradual increase in apparent R values with transport distance, where R values are low near the vent by fines depletion and high in distal areas because of fines enrichment. Using a least-squares fit of the variation in R with distance, we normalize R values for each sample to an intermediate distance of 20 km where the observed effect of fines enrichment matches fines depletion. Figure 16 shows these results and the calculated fluctuation between phreatomagmatic and magmatic eruptions in LM. We note that because vesiculation is observed in all LM samples, the term phreatoplinian is appropriate for their description (Self and Sparks, 1978). UM shows more uniform but generally lower R values than those of LM, indicative of UM's more constant but less pronounced phreatomagmatic character than that of LM. Overall, we believe that these data support field interpretations that LM varied between magmatic and phreatoplinian, while UM was mostly phreatomagmatic.

Transport

As described above, the NYT shows a variety of depositional textures suggestive of multiple modes of tephra dispersal and emplacement. Fallout layers are generally characterized by the coarsest mode (subpopulation 1). Pyroclastic flow/surge layers show a range for particle sizes including subpopulations 2 through 5 and bedding characteristics of traction (laminar beds) and saltation (dune beds) transport. Fine ash beds show bedding texture suggestive of deposition from suspended transport and are dominated by subpopulation 5 (Fig. 11). We have observed distinct variations in depositional textures as a function of transport distance that are described above as proximal and distal characteristics. A plot of subpopulation mode as a function of distance from the assumed vent locations is shown in Figure 17a. This plot shows the fallout subpopulation 1 generally fining with distance but also slightly coarsening at distances greater than 22 km, suggesting finer particles sticking to large particle surfaces, as microscopic observations show. Subpopulations 2 and 3 show a similar decrease in mode size with distance. These two subpopulations are found to be dominant in laminar bedded deposits likely to have been emplaced in a traction carpet. These subpopulations show no apparent effects of

aggregation, which might be explained by their continual attrition during grain flow. Subpopulation 4 has modes of appropriate size for saltation transport as supported by their prominence in dune beds. This subpopulation shows a slight fining with distance and a hint of coarsening by aggregation in distal sections. Subpopulation 5 is so fine (~5 ϕ), it most likely was carried by suspension, but it shows a distinct coarsening with distance, again likely caused by particle aggregation leading to its premature deposition.

A textural facies description has not yet been assigned from field observations. However, our granulometric data provide a basis for developing a hypothetical model in a similar fashion as described for the Cretaio Tephra (Orsi et al., 1992). This model entails definition of a development factor (= $1 + K + \gamma$), which combines the relative abundance (K) of each subpopulation and its degree of maturation (γ). Where a subpopulation has a high development factor, one may expect to see well formed bedding as a consequence. For example, dune development requires the presence of a significant fraction and sorting of a saltating population. Figure 17b shows variation of this development factor with transport distance. Saltation subpopulation 4 is best developed in proximal sections as evidence by observations at San Severino where dunes are well developed in ashy beds. In contrast, there are no apparent dunes at the most distal section (Sant' Angelo). As described by Orsi et al. (1991), planar bedded surges are most prominent in distal sections such as those at San Nicola la Strada and Sant' Angelo in Formis, which again support the general increase in development factor with distance for traction subpopulations 2 and 3. Fallout subpopulation 1 does not become developed until medial distances. We have found only one distinct fallout bed in proximal sections and deduce by stratigraphic relationships that others may have been eroded in those areas by successive ground-hugging surges. At distal sections, coarse fallout beds again are poorly represented. Suspended subpopulation 5 is shown in Figure 17b to be best developed at medial distances falling off in distal sections but still more developed than other subpopulations at Sant' Angelo (~34 km), again well recognized in field exposures.

DISCUSSION

In developing a reconstruction of the NYT eruption, we consider the results of data modeling described above in light of field observations. We contend that there is a close link among magma withdrawal, fragmentation, eruption dynamics, and composition. In developing our interpretations, we have to deal with some important uncertainties about vent(s) locations and the eruption column character. These uncertainties are addressed below.

The eruption likely took place in an environment with abundant water, very probably a shallow sea or a high water table. A hydrothermal system was apparently developed above the magma chamber as attested by the presence of hydrothermally altered lithic clasts in the tephra. Because the most proximal facies of the deposit are covered by younger rocks, it is not possible to define the characteristics of eruption phases, if any, prior to eruption of LM-1; hence, our assumption that it represents the first NYT eruption. Strong evidence for compositional stratification and volatile enrichment in the NYT magma chamber along with the development of a hydrothermal system above it suggests that the NYT magma chamber existed for some time prior to its eruption.

The NYT vent location is thought to be near a central point in the Phlegraean Fields area bounded by a curve encompassing UM deposits (Figure 1a). Further definition of the vent area is precluded by the scarcity of outcrops and their syndepositional erosion and deformation such that useable isopleth and isopach maps cannot be constructed. This problem is further compounded by the fact that maximum pumice and lithic fragment sizes do not regularly decrease with distance from the vent (Orsi et al., 1991). This observation suggests that complicated patterns of clast fallout are perhaps a consequence of the observed high ash-loading and moisture content in persistent phreatoplinian umbrella clouds. As a consequence, we have not been able to model eruption column heights and fluxes by the method of Carey and Sparks (1986).

Stratigraphy and grain size distributions have shown that varying eruptive and depositional mechanisms occurred during the emplacement of the NYT. The most striking variations are displayed by the contrasting textures between LM and UM products, although notable variations are also distinctly evident within each member. An additional complexity is that single eruptions apparently dispersed tephra by simultaneous fallout and flow/surge processes.

Because we do not have data that allows us to develop an eruption-column model based on fallout parameters, we develop quantitative eruption parameters from observations of tephra dispersal by pyroclastic flows/surges and the estimated values for water/magma mass ratios (R) of the phreatomagmatic eruptions. In order to model the dispersal data, we apply a numerical solution to the energy-line approach of Malin and Sheridan (1982). This solution is accomplished by using a version of the FLOW program of McEwen and Malin (1989) with a hypothetical preeruption topography constructed from the present-day slope of the Caserta plain and the Apennine scarp and an approximation of the location and size of the Phlegraean Fields caldera. This topography was digitized along a line extending from the center of the NYT

caldera (Lirer et al., 1987; Orsi et al., 1992) to a point near Sant' Angelo. The results constrain the initial pyroclastic surge/flow speeds required for LM pyroclastic surges/flows to reach a maximum runout distance of 34 km from the LM vent. Assuming Heim coefficients ranging from 0.05 to 0.30, the initial velocity of pyroclastic surges/flows (Figure 18a) is calculated (180 to 450 m/s), which allows constraint of the fountain height (2000 to 10,000 m) necessary to produce these velocities from the relationship $h = v^2/2g$ found appropriate for eruption column collapse by Dobran et al. (1992).

Eruption column parameters are also constrained by considering the variation of water/magma mass ratios (R) estimated for the phreatomagmatic phases ($R \approx 0.05$ to 0.7 from Figure 16). Using these values of R, the conversion ratio (CR) of the magma's thermal energy to kinetic energy of flow is estimated by the experimental relationships of Wohletz (1983) and McQueen et al. (1994). By equating this kinetic energy to $mv^2/2$, we find the eruptive column velocity as $v = (2 \text{ CR } C_p \Delta T)^{0.5}$, where $C_p = 1$ kJ/kg and $\Delta T = 900$. These velocity results (180 to 370 m/s) are shown in Figure 18b for LM where they correspond to those velocities determined as a function of Heim coefficient in the range of 0.05 to 0.2.

With the above estimations of eruption column behavior, we can make some further estimations of the central vent radius of LM eruptions. A similar estimation for UM is precluded by the ring-fracture nature of its vents where effective vent radius is very uncertain. For this exercise, we consider a range of eruption times from about 10 to 100 hours (by analogy to historic eruptions of similar magnitude), a DRE volume of 10 km^3 (LM mass eruption rates between 2.9 x 10^7 and 5.8 x 10^8 kg/s) expanded to a gas/pyroclast mixture volume by a factor of 330 to account for an average 2.7 wt% steam in LM eruption columns, and a range of vent velocities from 180 to 370 m/s, noted from Figure 18b. This calculation gives vent radii ranging from 70 to 300 m. The above predictions of fountain height and vent radii are quite compatible with column-collapse models presented by Wilson et al. (1980). Correlating LM's aspect ratio ($\approx$ 2 x 10^{-4}) to volumetric eruption rates discussed by Cas and Wright (1987) requires an eruptive duration of about 12 hours, setting LM vent radii in the range of 200 to 300 m. During the phreatoplinian to Plinian eruptions of LM, sustained column heights up to 38 km can be calculated for the mass fluxes cited above using the relationships of Wilson et al. (1978).

In order to compare LM and UM eruptions, we apply R values determined from the granulometric analysis to calculate column velocities and collapse heights. For this case Heim coefficients are estimated by dividing collapse height by pyroclastic flow/surge runout distances (34 km for LM, 14 km for UM). The comparison (Fig. 19b) shows LM pyroclastic flows/surges having greater mobility (Heim coefficients averaging 0.14) and greater collapse heights

(averaging > 4 km) than UM (averaging 0.20 and < 3 km, respectively). While several UM eruptive phases apparently produced high collapse heights, they also apparently involved lower water/magma ratios than UM eruptions of similar collapse heights, which may explain their higher Heim coefficients. These results generally explain the greater runout distances of LM products.

Now that we have developed some quantitative bounds for the NYT eruption, we offer a qualitative interpretation illustrated in Figure 20. The first eruptive events were apparently triggered by influx of new trachytic magma (eventually erupted as UMt) into the preexisting chamber. Eruptions began with the tapping of the uppermost compositionally evolved, volatile- and likely bubble-rich, LMat layer of magma. These eruptions comprise a series of explosions driven by wet water/magma interaction that produced LM-1. During its ascent, bubbles in LMat grew and likely began to coalesce just prior to encountering ground water, hence the resulting interaction with the ground water was likely stimulated by magmatic fragmentation. Further significant interaction with sea water was limited by high speed movement of the tephra through the upper portions of the conduit. Laden with fine ash and steam generated by ground water vaporization, the resulting eruption columns partially collapsed producing surge clouds that displayed high mobility, traveling over distances of about 34 km. In doing so, the surges had to surmount a low topographic barrier of pre-NYT vents in the Phlegraean Fields. The high mobility of these surges can be attributed to their production from collapse of very high eruption column fountains. Additionally for most of their runout, the surges moved on a smooth surface, likely covered by marshes and gently dipping toward the Apennines. Partial vaporization of this marsh water may have introduced additional momentum into the surges and sustained their movement.

After the LM-1 eruptions, the character of NYT eruptions abruptly changed. Trachytic magma (LMt) erupted following a repeated pattern determined by regular fluctuations in the availability of water to the conduit. The change in eruptive character is born out by the greatly differing depositional characteristics of LM-2 compared to those of LM-1. An apparent time break between deposition of LM-1 and LM-2 (marked by an erosional break concurrent with partial caldera collapse) must have allowed water to only partly refill the cone of depression in the aquifer left by the LM-1 eruption. Even though the new vesiculated LMt magma interacted with a smaller amount of water than did LMat (LM-1), its viscosity was lower and R value more optimum such that its fragmentation was just as efficient, producing highly energetic phreatoplinian explosions. This eruption apparently flushed the water out of the conduit so that during the following eruption of LM-3, vesiculated rising magma did not encounter a significant amount of water until it reached the sea floor. Only the upper part of LM-3 magma interacted

efficiently with the sea water and was disrupted in fine particles, while the lower part was mainly fragmented by exsolution of the magmatic gases. The phreatoplinian LM-2 to mostly magmatic eruption of LM-3 defines a trend repeated a total of six times after eruption of LM-1.

The phreatoplinian explosions of LM-2, LM-4, LM-6, LM-8, LM-10, and LM-12 generated columns that partially collapsed, giving rise to surge emplacement in proximal areas, while the convective part of the columns rose high to form an umbrella cloud that deposited ash fallout in both proximal and distal areas. Accretionary lapilli were abundant in these phreatoplinian eruption clouds due to high amount steam present.

In contrast, more magmatic (phreatoplinian to Plinian) eruptions of LM-3, LM-5, LM-7, LM-9, LM-11, and LM-13 generated columns that did not collapse but dispersed in downwind plumes of pumice laden with fine ash and steam experiencing premature ash fallout with the formation of accretionary lapilli. The resulting pumice-and-ash fall layers show anomalous areal distribution of maximum pumice and lithic components perhaps due to the complicated fallout dynamics inside the relatively dense and turbulent umbrella cloud. Accretionary lapilli occur in the fine-grained upper part of the pumice-and-ash fallout deposit. Some of them are comparable in size with the underlying pumice fragments. Considering their higher density, this relationship indicates that significant growth of the accretionary lapilli did not occur until after pumice fallout.

Each phreatoplinian explosion tapped all three magma layers of the chamber, whereas the phreatoplinian to magmatic explosions only drained the intermediate trachytic layer. Increase in withdrawal depth, evidenced by syneruptive commingling of all three layers of the chamber (Spera, 1984), can be attributed to a dramatic pressure decrease on the magma beneath the conduit and/or a large increase in eruptive mass flux, both consequences of the water/magma interaction during phreatoplinian explosions. Hence magma chamber chemical zonation is not be displayed by products of this type of eruption.

A time break occurred after LM eruptions, and then activity resumed with very different characteristics in UM eruptions. The time break is marked by initiation of a caldera collapse and a change from central-vent to ring-fracture eruptions. This change in vent character caused an overall pressure decrease on the chamber and therefore a lateral elongation of the evacuation isochrons (Spera, 1984) that allowed the UMat magma previously trapped in the chamber top to be erupted. The eruption then continued with the extraction of the deepest magma in the chamber (UMt). Although UM products show slightly higher percentages of phreatomagmatic components than do LM products, the efficiency of the interactions was apparently lower.

During this phase, explosions generated lower fountains (than LM) feeding pyroclastic flows and surges that had to surmount newly formed caldera topography. The caldera likely continued to collapse after the end of the eruption, as suggested by the absence of any outcrop of the NYT in the central part of the Phlegraean Fields.

CONCLUSIONS

The NYT consists of two members, LM and UM, representing products of two eruptive phases, respectively: (1) initial, central-vent, mostly phreatoplinian eruptions dispersed tephra over an area of at least 1000 km^2 and (2) caldera collapse with mostly phreatomagmatic eruptions that dispersed tephra over 250 km^2. Both members show compositional gradients from alkali trachyte to trachyte with UM showing late stage latitic compositions. Estimation of magma densities, viscosities, and volatile contents of the NYT products help us distinguish three separate magmas that can neither be related by simple crystal fractionation nor modeled by simple inversion of magma chamber stratification. These three magma compositions, however, are related to changes in eruptive styles and tephra dispersal as observed in the field, which can be explained by estimated variations of density, viscosity, and volatile content with time. For example, we have found an apparent general increase in density, decrease in viscosity, and decrease in magma fragmentation depth during the course of eruption of each member. Tephra grain-size distributions reflect a combination of magmatic and phreatomagmatic fragmentation with dispersal in pyroclastic flows, surges, and fallout. Modeling of grain-size data by sequential fragmentation/transport theory allows us to discriminate the relative roles of magmatic and phreatomagmatic fragmentation as eruptions progressed, as well as variation in transport mechanism as a function of distance from the vent. Overall, LM shows a larger range of water/magma mass ratios than does UM. Combination of dispersal range data and eruptive energies predicted by water/magma ratios shows that LM produced higher average fountain heights than those of UM. For estimated vent radii in the range of 200 to 300 m, the extrusion of 10 km^3 (DRE) of LM tephra required about 12 hours. UM shows volumes about three times that of LM but was apparently erupted from multiple ring vents; hence, the eruption duration of this member was likely as long and perhaps longer than that of LM. An important conclusion of this study is a demonstrated correspondence of magma composition and eruption dynamics. This relationship suggests that the interaction of sea water/ground water with magma greatly influenced discharge rates and hence the depth of withdrawal and degree of magma commingling during eruption.

ACKNOWLEDGMENTS

Appendix A. Detailed Description of LM Deposits

LM-1 is a gray to brown layer of vesicular ash, composed of many millimeter- to centimeter-thick laminae varying in grain size from ash to coarse ash and generally capped with a dark gray ash bed. Its maximum thickness is ~90 cm at Quarto and Ponti Rossi. At San Severino, 3 km beyond the Phlegraean caldera scarp, its thickness abruptly decreases to 30 cm, beyond which it gradually thins over a distance of 30 km to 7 cm at Sant' Angelo in Formis (excluding debris flows of LM-1 material). This layer often shows cross lamination and erodes the underlying paleosol. Load deformation and slumping are quite common. Field characteristics suggest that most of the beds were deposited by surge clouds.

LM-2 is a massive, gray to light brown ash layer with scattered hydrothermally altered lithic clasts. In some cases its emplacement eroded and/or deformed the top of LM-1. Its thickness decreases from 27 cm at San Severino to 2 cm at Sant' Angelo in Formis. Accretionary lapilli, some of which are larger than one centimeter, are dispersed throughout all the exposures of this layer with exception of that at Sant' Angelo in Formis. Variation in thickness from proximal to intermediate areas could have been caused by deposition from a number of surge clouds not all reaching intermediate and distal locations; different surge beds are obvious only at Quarto. While field evidence suggests that the layer was mostly deposited by surge clouds close to the vent, LM-2 is an ash-fallout in distal areas.

LM-3 is a zoned pumice-and-ash-fallout deposit. The lower part contains pumice and lithic fragments. White-to-gray pumice is angular and normally graded. Lithic clasts are angular, composed of dark gray lava, sometimes brown or reddish from hydrothermal alteration. The upper part is composed of ash and accretionary lapilli, often very abundant and partially coalesced forming a vesiculated tuff. This layer is found in areas extending from Scarafea, where it attains a thickness of 11 cm, to Sant' Angelo in Formis, where it is 5 cm thick. In more proximal exposures (*i.e*., San Severino) it is eroded by the overriding LM-4.

LM-4, recognized only at Scarafea to Sant' Angelo in Formis, changes in textural and sedimentological characteristics with distance from the vent. At Scarafea it includes three ash beds, containing accretionary lapilli and angular pumice fragments in different proportions, while at Quadrivio di Ischitella it is an ash bedset, free of accretionary lapilli with very crude lamination, and at the most distal exposure, it is a single thin massive ash bed. The thickness of the layer varies from 24 cm, at Scarafea, to 2 cm, at Sant' Angelo in Formis. Accretionary lapilli although not always very evident, are concentrated in the upper parts of each bed. Pumice fragments are scattered in the middle and lower part of the layer and concentrated in its uppermost part due to sinking from the overlying LM-5. Dark lava and minor pinkish hornfels lithic clasts are scattered throughout the layer. While the proximal deposits are best described as surge beds, the distal equivalent is interpreted as an ash fallout.

LM-5 occurs from San Severino to Sant' Angelo in Formis. Its thickness, which reaches a maximum value of 8 cm at San Severino, usually does not exceed the dimension of one pumice, and varies from 3.5 to 1 cm with increasing distance from the vent. The layer is composed of angular, white-to-brown, pumice fragments and ash. At San Severino, ash abundance largely dominates subangular pumice and could be the deposit of an ash surge that incorporated and transported falling pumice fragments. In distal areas this layer is interpreted as a pumice-and-ash fallout deposit.

LM-6 is a light gray ash layer occurring over the whole NYT outcrop area. From San Severino to Quadrivio di Ischitella, over a distance of 12 km, its sedimentological and textural characteristics change significantly. At San Severino it is composed of discrete ash beds with a variable amount and distribution of accretionary lapilli and pumice fragments. From Quadrivio di Ischitella to Sant' Angelo in Formis it is a massive ash bed. Wet clumps of ash are present in this layer. At Scarafea it shows scarce, small and scattered vesicles, and its thickness decreases from 26 to 12 cm over a distance of 100 meters as the substrate elevation increases. Field evidence suggests that the layer is mostly an ash fallout bed in distal areas, and a sequence of surge and ash fallout beds in proximal areas.

LM-7 is similar to LM5. It consists of an alignment of angular pumice fragments in intermediate and distal areas and of an ash bed with angular pumice fragments in the proximal area. In some of the most distal exposures LM-7 is only represented by a thin vesiculated tuff, interpreted as a pumice-and-ash fallout deposit.

LM-8 is a gray ash layer cropping out from Scarafea to the most distal areas. Fluctuating in thickness and eroded by LM-10 in more proximal exposures, it is composed of a variable number of massive ash beds with accretionary lapilli and dispersed pumice fragments. At Quadrivio di Ischitella and San Nicola La Strada it comprises a few beds separated by alignments of vesicles. In both outcrops the uppermost layer has both textural characteristics and thickness comparable with those of the same layer in other outcrops. This layer is interpreted as consisting of ash fallout and surge beds that were not deposited homogeneously over the whole outcrop area.

LM-9 is a single bed of angular pumice fragments, lithic clasts, and ash particles, showing variable thickness that generally decreasing from 5 cm at Quadrivio di Ischitella to 2 cm at Sant' Angelo in Formis. At Scarafea, which is the most proximal outcrop of this layer, it has been partially eroded by the overriding LM-10 surge. Pumice fragments are white to gray, according to degree of vesicularity. The lithic fragments are of black lava, sometimes brownish from alteration. All the components show normal grading although the boundary between the lower coarser part and the upper finer part of the bed is well marked. The layer is interpreted as a pumice-and-ash-fallout deposit.

LM-10 changes in characteristics significantly with distance from the vent. In very distal areas it is composed of a single, gray ash bed with many accretionary lapilli. In less distal and intermediate areas (Casaluce, Quadrivio di Ischitella, Scarafea) fine- and coarse-grained plane parallel and cross laminated beds are also present. In the most proximal outcrops (San Severino) the layer is composed of a succession of undulating ash beds with accretionary lapilli. The thickness of the layer varies from 80 to 20 cm from San Severino to Sant' Angelo in Formis. The massive ash deposit in distal area is interpreted as an ash fallout bed whereas the proximal laminated or undulating deposits are considered surge beds.

LM-11 is composed of angular pumice, lithic fragments and fine particles. Its thickness varies from 7 to 4 cm from Ischitella to Sant' Angelo in Formis. A partially eroded fallout bed at San Severino represents its most proximal outcrop. The pumice fragments are white and gray. The lithic clasts are black lavas, sometimes altered to brownish or reddish, and brown tuff. The layer is a pumice-and-ash-fallout deposit.

LM-12 is a single, massive, gray, ash-fallout bed. It also contains accretionary lapilli and scattered small and angular pumice fragments. The thickness gradually decreases from 8 to 2 cm from Scarafea to Sant' Angelo in Formis. The possibility that this layer is genetically related to LM-11 and represents the later ash fallout cannot be ruled out. In this case LM-11 plus LM-12 would represent a pumice-and-ash-fallout deposit.

LM-13 is a single bed composed of white to gray pumice and lithic fragments with a normal to reverse symmetric grading. Its thickness decreases from 14 to 9 cm from Scarafea to Sant' Angelo in Formis. The lithic clasts are of black lavas, sometimes brownish and reddish for alteration, and brown tuff. The layer is a pumice-and-ash-fallout deposit although it contains a smaller proportion of fine particles than the other pumice-and-ash-fallout beds of the succession.

Appendix B. Magma Chamber Model

The compositional variations displayed by the studied rocks allow the NYT magma chamber to be modeled as a three-layer system: an uppermost alkali trachyte, an intermediate trachyte and a lowermost trachyte-to-latite. The magmas of the three layers are not related by simple fractional crystallization, but they are distinct magma batches that only partially mixed during eruption. Orsi et al. (1992) show that the NYT sequence cannot be modeled as an inverted compositionally zoned magma body with magma composition becoming more basic during the course of the eruption. The changes in composition of the erupted magmas match changes in eruption mechanisms and likely in magma chamber withdrawal dynamics. Transition from phreatoplinian (LM) to mostly phreatomagmatic (UM) eruptive phase is accompanied by a change in magma composition from trachyte to alkali trachyte. This last magma batch, likely trapped near the roof of the chamber during the LM eruptive phase, was tapped at the beginning of UM phase, probably in relation to change from central-vent to ring-fractures eruption that followed the beginning of a caldera collapse (Orsi et al., 1991). Water vaporization in the conduit system during the phreatoplinian phases may have stimulated withdrawal of magma from greater depths in the chamber by an increase in mass flux and

decrease in pressure in the conduit (Blake and Ivey, 1986). Therefore magmas over a wider range of depth were tapped concurrently and mixed during their ascent.

At the beginning of the NYT eruption, the first magma tapped from the chamber was LMat that generated LM-1. As the eruption continued, trachytic magma beneath the alkali trachyte was also tapped with the initiation of phreatoplinian activity and the two magmas mixed during their ascent in the conduit. With the transition from central-vent to ring-fracture eruption, the roofward trapped alkali trachyte (UMat) was again tapped. During the later stages of the eruption a geochemically distinct trachytic magma (UMt) was tapped. UMt displays a variation of chemical composition that overlaps the LMt compositional range. Zonation time for chambers of less than 100 km^3 requires on the order of 10^3-10^4 years (Wolff et al., 1990), thus UMat must have differentiated before entering the chamber, otherwise its lighter differentiated part would have mixed with the overlying trachyte.

Appendix C. Interpretation of LOI Values

The facts that the magma degasses during eruption, and that glassy products can hydrate during and after emplacement, begs the question of legitimacy of our assumption about LOI values. A numerical study of magma degassing during phreatomagmatic eruption (Wohletz, 1994) shows the dominating controls of rapid tephra quenching. For even modest water/magma ratios of 0.1 and fragmentation depths $\leq$ 200 m, <25% of the magmatic volatile can degas before being tephra quenching to temperatures of 100°C. Furthermore, Wohletz (1994) shows that subsequent post-emplacement hydration of pumice should not have exceeded 1 wt% over the 12 ka since eruption of the NYT. In further support of interpreting LOI data for the NYT eruptions, Wörner et al. (1987) present stable isotope supporting primary volatile retention by the phreatomagmatic Laacher See tephra, and Dunbar and Kyle (1989) demonstrate glass inclusion data for the phreatomagmatic Hatepe tephra that lie on the same Cl-H_2O correlation line as described for the Taupo eruption. The NYT, as we show, is clearly phreatomagmatic, thus lending credence to utilization of LOI values. While this assumption about the meaning of LOI for the NYT samples can only be considered semi-quantitative, it is this relative variation in H_2O content that is useful in demonstrating that magma composition changes with observed variations in dispersal and stratigraphic character. Below, we show some interesting correlations of eruption variations based on these LOI data, but in light of their uncertain meaning, we do not draw them into our subsequent conclusions.

Appendix D. Chemical Modeling Technique

In calculating bulk densities, a major modification of Bottinga and Weill's (1970) method involved taking into consideration the volume concentration of phenocrysts and vesicles and their respective densities. Under the assumption that the major volatile component is water and that its relative abundance in the magma is represented by LOI values, its solubility in the magma was estimated as a function of silica content. Assuming endmember basalt (SiO$_2$ = 45 wt%) and rhyolite (SiO$_2$ = 75 wt%) compositions, the water solubility functions of pressure (Sparks, 1978) were combined to give

$$x_w = x_r \left[\frac{x_{Si} - 45}{30} \right] + x_b \left[\frac{75 - x_{Si}}{30} \right] \quad . \tag{D-1}$$

For this approximation x_r = the solubility of water in rhyolite in wt% (x_r = 0.13 $p^{0.5}$), x_b = the solubility of water in basalt (x_b = 0.0215 $p^{0.7}$), x_{Si} = wt% silica, and p = pressure in bars. The partial molar volumes of the oxides are given by Bottinga and Weill (1970) for a range of temperatures between 1250 and 1600 °C, which were linearly extrapolated to 900 °C for application to our magma temperatures. Compatible with cgs values used by Bottinga and Weill (1970), we fit a third-order polynomial to partial molar water volume data (Burnham et al., 1969):

$$V_w = 24.7 + \left[0.007(T - 900) \right] - 1.5 p_k + 0.084 p_k^2 - 0.0014 p_k^3 \quad . \tag{D-2}$$

In Eq. (2) V_w = the partial molar volume of water in solution in a silicate melt, T = temperature (°C), and p_k = pressure in kilobars. Using Eq. (D-1), the amount of water in excess of saturation as a function of pressure could be estimated, which allows the calculation of water vapor volume as a function of pressure and temperature. For temperatures between 700 and 1200 °C and pressures up to 1 kbar, water vapor volume can be approximated as

$$V_v = \frac{4489 + 4.615(T - 700)}{p} \qquad \text{(D-3)}$$

where V_v is in cm^3/g and p = pressure in bars. In this manner the volume fraction of water-vapor vesicles was calculated for the magmas. Where this volume fraction reached 0.75, we assume that the magma was at its fragmentation surface at depth in the conduit. In order to compensate for some adiabatic cooling of the water vapor above the fragmentation surface, we simply calculated V_v as $3565/p$ which is appropriate for T = 500 °C.

Both the viscosity algorithms given by Bottinga and Weill (1972) and Shaw (1972) were applied to magma compositions with the former giving a lower viscosity range sensitive to temperature only and the latter an upper range, which is sensitive to pressure and temperature as well as water content. Bottinga and Weill's (1972) method was modified to use simple linear extrapolations of Newtonian viscosity coefficients as functions of temperature and the Einstein-Roscoe equation (McBirney and Murase, 1984) for estimation of the effect of phenocryst and vesicle suspension. For Shaw's (1972) method, we follow viscosity estimation suggested by McBirney and Murase (1984), who adapted a suspension effect on viscosity from Sherman (1968); we note that phenocryst suspension effects are small for the NYT magmas but that vesicle presence is nonetheless very important.

Appendix E. Granulometric Modeling Technique

Granulometric data were acquired by dry sieving at full-phi (ϕ) intervals from -5 to 7ϕ. While pumice samples are fresh, fine ash samples showed varying degrees of zeolitization by analcime (de Gennaro, personal communication) for which sample disaggregation was required. Fifty g aliquots of sample were treated with about 100 ml of dilute HCl for 5 minutes in an ultrasonic bath. One liter of distilled water was added to further dilute the acid and left for 24 hours to let the particles settle. After drainage of the dilute acid, the samples were dried overnight at 150°C. This treatment has also produced partial disaggregation of some of the accretionary lapilli present in many samples. The samples were then mechanically sieved between -5 and 3ϕ. The fraction finer than 3ϕ was analyzed using a Coulter counter (Allen, 1981) at the Dipartimento Geomineralogico of the University of Bari.

In analysis of granulometric data, we have applied the sequential fragmentation/transport (SFT) theory of Wohletz et al. (1989), which models observed grain-size distribution data by addition of theoretical subpopulation distributions whose mode, sorting, and skewness are functions of a unique physical parameter, gamma (γ). SFT derives its physical basis from the concept that particle-size distributions in nature evolve from a sequence of mechanical events that produce smaller fragments from larger ones and subsequently sort the fragments by size by one or more transport processes. This concept is explicitly stated as

$$n(x,m) = c \int_0^m \int_{x-\xi}^0 n(x',m')\Phi(m' \rightarrow m)p(\xi)dx'\,dm' \qquad , \qquad \text{(E-1)}$$

in which $n(x,m)$ = the number of fragments of mass m found at location x, c = constant, x' and m' = the parental source location and particle mass, respectively, $\Phi(m' \rightarrow m)$ = the transfer function that expresses the physical mechanism of fragmentation in which parental masses (m') are broken into smaller daughter masses (m), and $p(\xi)$ = the probability of a particle arriving at some location x as a function of the transport mechanism. Wohletz et al. (1989) have found a general solution to Equation (4), which is based on the assumption that both fragmentation and transport physics are sensitive to mass (as can be expressed by equations of conservation of mass, momentum, and surface free energy). The mass sensitivity of fragmentation and transport are expressed by a mass sensitivity exponent γ, which is related to sorting (see Wohletz et al., 1989), and with conversion of Equation (E-1) number distribution to a size distribution, the general solution is

$$\frac{dM}{d\phi} = K\delta^6 \exp\left[-\frac{x}{\xi_0}\frac{\delta^{3(\gamma+1)}}{(\gamma+1)}\right] ,$$ (E-2)

for which $dM/d\phi$ = the mass of particles per phi size interval, the constant K = 1 for distributions = 100 wt%, δ = particle diameter, and x/ξ_0 = the normalized sample location (= 1 for geological applications). The distribution expressed by Equation (5) is similar to the lognormal and Weibull distributions, but it has physical significance. With the conversion of the mass distribution of Equation (4) to a size distribution, Wohletz et al. (1989) considered particle shape and density variations in tephra samples and a general solution that requires the addition of two or more distributions predicted by Equation (E-2), each with specific γ and K values (<1).

In applying Equation (E-2), we numerically invert sample distribution data to find SFT parameters that reproduce at least 95% of the observed sample distribution variance (indiscernibly different by visual inspection). While this data inversion technique is not numerically unique, the constraints of pyroclast and deposit textures narrows the range of possible solutions to a point where their variations are statistically insignificant. From this inversion, we find distribution subpopulation modes and dispersion (γ) parameters that link the subpopulations to their physical mechanism of formation (fragmentation/aggregation dependent upon magmatic and hydromagmatic eruption) and transport mechanism (ballistic, suspension, saltation, and traction). The SFT procedure is implemented by a user interactive computer program (SEQUEN) described by Wohletz et al. (1989). SFT parameters of subpopulation mode, dispersion (γ), and fraction (K) were tabulated and plotted in order to see trends throughout the stratigraphic sequence.

REFERENCES

Alessio, M., Bella, F., Belluomini, G., Calderoni, G., Cortesi, C., Fornaseri, M., Franco, M., Improta, F., Scherillo, A. and Turi, B., 1971. Datazioni con il metodo del C-14 di carboni e livelli humificati (paleosuoli) intercalati nelle formazioni piroclastiche dei Campi Flegrei (Napoli). Rend. Soc. It. Miner. Petrol., 27, 2: 305-317.

Alessio, M., Bella, F., Improta, S., Belluomini, G., Cortesi, C. and Turi, B., 1973. University of Rome Carbon-14 dates IX. Radiocarbon, 13: 395-411.

Alessio, M., Bella, F., Improta, S., Belluomini, G., Calderoni, G., Cortesi, C. and Turi, F., 1974. University of Rome C-14 dates XII. Radiocarbon, 16: 3-358.

Allen, T., 1981. Particle size measurement. Chapman and Hall, 678 pp.

Armienti, P., Barberi, F., Bizouard, H., Clocchiatti, R., Innocenti, F., Metrich N., Rosi, M. and Sbrana, A., 1983. The Phlegraean Fields: magma evolution within a shallow chamber. In: Explosive Volcanism. (Barberi, F. and Sheridan, M., Editors) J. Volcanol. Geotherm. Res., 17: 289-311.

Barberi, F., Innocenti, F., Lirer, L., Munno, R., Pescatore, T. S. and Santacroce, R., 1978. The Campanian Ignimbrite: a major prehistoric eruption in the Neapolitan area (Italy). Bull. Volcanol., 41-1: 10-22.

Barberi, F. Cassano, E., La Torre, P., and Sbrana, A., 1991. Structural evolution of Campi Flegrei caldera in light of volcanological and geophysical data. J. Volcanol. Geotherm Res., 48: 33-49.

Blake, S. and Ivey, G. N., 1986. Magma mixing and the dynamics of withdrawal from stratified reservoirs. J. Volcanol. Geotherm. Res., 27: 153-178.

Bottinga, Y. and Weill, D. F., 1970. Densities of liquid silicate systems calculated from partial molar volumes of oxide components. Amer. J. Sci., 269: 169-182.

Bottinga, Y. and Weill, D. F., 1972. The viscosity of magmatic silicate liquids: a model for calculation. Amer. J. Sci., 272: 438-473.

Breislak, S., 1801. Voyage physiques et litologiques dans la Campanie. Paris.

Branney, M. J., 1991. Eruption and depositional facies of the Whorneyside Tuff Formation, English Lake District: an exceptionally large-magnitude phreatoplinian eruption. Geol. Soc. Am. Bull., 103: 886-897.

Burnham, C. W., Holloway, J. R., and Davis, N. F., 1969. Thermodynamic properties of water to 1000ºC and 10,000 bars. Geol. Soc. Amer. Spec. Pap. 132: 96 pp.

Capaldi, G., Civetta, L., Di Girolamo, P., Lanzara, R., Orsi, G. and Scarpati, C., 1987. Volcanological and geochemical constraints on the genesis of the deposits of Yellow Tuff in the Neapolitan-Phlegraean area. Rend. Acc. Sc. Fis. Mat. Napoli, Sp. Issue: 25-40.

Carey, S. and Sparks, R. S. J., 1986. Quantitative models of the fallout and dispersal of tephra from volcanic eruption columns. Bull. Volcanol., 48: 109-125.

Cas, R. A. F. and Wright, J. V., 1987. Volcanic successions: modern and ancient. Allen & Unwin, London, 528 pp.

Cassignol, C. and Gillot, P. Y., 1982. Range and effectiveness of unspiked potassium-argon dating: experimental ground work and application. In: Odin, G. S. (Ed.), Numerical Dating in Stratigraphy, Wiley, New York, 160 pp.

Cita, M. B., Vergnaud-Grazzini, C., Robert, C., Chambley, H. Ciaranfi, N., and D'onofrio, S., 1977. Paleoclimatic record of a long deep sea core from the eastern Mediterranean. Quat. Res., 8: 205.

Cole, P.D. and Scarpati, C., 1993. A facies interpretation of the eruption and emplacement mechanisms of the upper part of the Neapolitan Yellow Tuff, Campi Flegrei, southern Italy. Bull. Volcanol., 55: 311-326.

Deino, A., Curtis, G., and Rosi, M. 1992. ^{40}Ar/^{39}Ar dating of the Campanian Ignimbrite. Campanian Region, Italy. Intern. Geol. Congress, Kyoto, Japan, Abstr. Vol. 3: 633.

De Lorenzo, G., 1904. L' attività vulcanica nei Campi Flegrei. Rend. Acc. Sc. Fis. Mat., 10: 204-221.

Di Girolamo, P., Ghiara, M. R., Lirer, L., Munno, R., Rolandi, G. and Stanzione, D., 1984. Vulcanologia e petrologia dei Campi Flegrei. Boll. Soc. Geol. It., 103: 349-413.

Dobran, F., P. 1992. Nonequilibrium flow in volcanic conduits and application to the eruptions of Mt. St. Helens on May 18, 1980, and Vesuvius in AD 79. Jour. Volcanol. Geotherm. Res., 49: 285-311.

Dobran, F., Neri, A., and Macedonio, G., 1992. Numerical simulation of collapsing volcanic columns. C.N.R.-Gruppo Nazionale per la Vulcanologia, VSG Report 92-2, Giardini, Pisa, 49 pp.

Dunbar, N. W., Hervig, R. L., and Kyle, P. R., 1989. Determination of pre-eruptive H_2O, F, and Cl contents of silicic magmas using melt inclusions: examples from Taupo volcanic center, New Zealand. Bull. Volcanol., 51: 177-184.

Dunbar, N. W., and Kyle, P. R., 1989. Volatile contents of obsidian from the Taupo volcanic zone, New Zealand, and implications for eruption processes. New Mexico Bur. Mines & Min. Res. Bull. 131: 77.

Falini, F. 1950. Rilevamento geologico della zona nord-occidentale dei Campi Flegrei. Boll. Soc. Geol. It., 69: 212-264.

Fisher, R. V., 1983. Flow transformations in sediment gravity flows. Geol., 11: 273-274.

Fuhrman, M. L. and Lindsley, D. H., 1988. Ternary-feldspar modeling and thermometry. Amer. Mineral., 73: 201-215.

Kushiro, I., 1986. Viscosity of partial melts in the upper mantle. Jour. Geophys. Res., 91: 9343-9350.

Lange, R. A. and Carmichael, I. S. E., 1987. Densities of Na2O-K2O-CaO-MgO-FeO-Fe2O3-Al2O3-TiO2-SiO2 liquids: New measurements and derived partial molar properties. Geochim. Cosmochim. Acta, 51: 2931-2946.

Lirer, L. and Munno, R., 1975. Il tufo giallo napoletano (Campi Flegrei). Per. Mineral., 44: 103-118.

Lirer, L., Luongo, G. and Scandone, R., 1987. On the volcanological evolution of Campi Flegrei. EOS, 68, 16: 226-233.

Lucini, P. and Tongiorgi, E.,1959. Determinazioni con il C-14 di un legno fossile dei Campi Flegrei (Napoli). Studi e Ricerche Divis. Geominer. C.N.E.N., Roma, 2: 215-226.

Malin, M. C. and Sheridan, M. F., 1982. Computer-assisted mapping of pyroclastic surges. Sci., 217: 637-640.

McBirney, A. R., and Murase, T., 1984. Rheological properties of magmas. Ann. Rev. Earth Planet. Sci., 12: 337-357.

McEwen, A. and Malin, M. C., 1989. Dynamics of Mount St. Helens' 1980 pyroclastic flow, rockslide-avalanche, lahars, and blast. J. Volcanol. Geotherm. Res., 37: 205-231.

McMillan, P. F. and Holloway, J. R., 1987. Water solubility is aluminosilicate melts. Contrib. Mineral. Petrol., 97: 320-332.

McQueen, R. M., Wohletz, K. H., and Morrissey, M. M., in press, Experimental study of hydrovolcanism by fuel-coolant analogs. Los Alamos National Laboratory rept., LA-UR-94-0370: 1-79.

Nicotera, P., 1950. Osservazioni geologiche sulla collina di Posillipo e sulla zona urbana occidentale di Napoli. Boll. Soc. Geolog. Ital., 69: 335-362.

Orsi, G. and Scarpati, C., 1989. Stratigrafia e dinamica eruttiva del Tufo Giallo Napoletano. Boll. GNV, 2: 917-930.

Orsi, G., Civetta, L., Aprile, A., D'Antonio, M., de Vita, S., Gallo, G., Piochi, M., 1991. The Neapolitan Yellow Tuff: eruptive dynamics, emplacement mechanism and magma evolution of a phreatoplinian-to-plinian eruption. In: Orsi, G. and Rosi, M. (Editors), Large ignimbrite eruptions of the Phlegraean Fields caldera: the Neapolitan Yellow Tuff and the Campanian Ignimbrite, Workshop on explosive volcanism, Napoli, September 1-8, guidebook.

Orsi, G., D'Antonio, M., de Vita, S. and Gallo, G., 1992. The Neapolitan Yellow Tuff, a large-magnitude trachytic phreatoplinian eruption: eruptive dynamics, magma withdrawal and caldera collapse. J. Volcanol. Geotherm. Res., 53: 275-287.

Papale, P., and Dobran, F., 1992. Modeling of the ascent of magma during the plinian eruption of Vesuvius in AD 79. C.N.R.-Gruppo Nazionalle per la Vulcanologia, V. S. G. Report 92-1, Giardini, Pisa, 51 pp..

Rittmann, A., 1950. Sintesi geologica dei Campi Flegrei. Boll. Soc. Geol. It., 69: 117-128.

Rosi, M., Sbrana, A. and Principe, C., 1983. The Phlegrean Fields: structural evolution, volcanic history and eruptive mechanism. J. Volcanol. Geotherm. Res., 17: 273-288.

Rosi, M. and Sbrana, A., 1987. The Phlegrean Fields. CNR, Quaderni de "La Ricerca Scientifica", 114, 175 pp.

Scarpati, C., Cole, P., and Perotta, A., 1993. The Neapolitan Yellow Tuff - A large volume multiphaase eruption from Campi Flegrei, Southern Italy. Bull. Volcanol., 55: 343-356.

Scherillo, A. and Franco, E., 1967. Introduzione alla carta stratigrafica del suolo di Napoli. Atti Acc. Pontaniana, Napoli, 16: 27-37.

Self, S. and Sparks, R. S. J., 1978. Characteristics of widespread pyroclastic deposits formed by the interaction of silicic magma and water. Bull. Volcanol., 41: 196-212.

Self, S., 1983. Large scale phreatomagmatic silicic volcanism: a case study from new Zealand. J. Volcanol. Geotherm. Res., 17: 433-469.

Shaw, H. R., 1972. Viscosities of magmatic silicate liquids: an empirical method of prediction. Amer. J. Sci., 272: 870-893.

Sheridan, M. F. and Wohletz, K. H., 1983. Hydrovolcanism: basic considerations and review. J. Volcanol. Geotherm. Res., 17: 1-29.

Sherman, P., 1968. Emulsion Science. Academic, New York, 351 pp.

Sparks, R. S. J., 1978. The dynamics of bubble formation and growth in magmas: A review and analysis. J. Volcanol. Geotherm. Res., 3: 1-37.

Spera, F. J., 1984. Some numerical experiments on the withdrawal of magma from crustal reservoirs. J. Geophys. Res., 89: 8222-8236.

Ventriglia, U., 1950. Rilievo geologico dei campi flegrei (zona centrale fra la direttissima Napoli-Roma e la collina dei Camaldoli). Boll. Soc. Geolog. Ital., 69: 265-334.

Vighi, L., 1950. Rilevamento geologico della zona a Sud del parallelo di Baia e della zona di Nisida, Coroglio e Trentaremi, nei Campi Flegrei. Boll. Soc. Geolog. Ital., 69: 179-210.

Walker, G. P. L., 1971. Grain-size characteristics of pyroclastic deposits. J. Geol., 79: 619-714.

Walker, G. P. L., 1981. Characteristics of two phreatoplinian ashes, and their water flushed origin. J. Volcanol. Geotherm. Res., 9: 395-407.

Walker, G. P. L., 1983. Ignibrite types and ignimbrite problems. J. Volcanol. Geotherm. Res., 17: 65-88.

Wilson, L., Sparks, R. S. J., Huang, T. C., and Watkins, N. D., 1978. The control of volcanic column heights by eruption energetics and dynamics. J. Geophys. Res., 83: 1829-1836.

Wilson, L., Sparks, R. J. S., and Walker, G. P. L., 1980. Explosive volcanic eruptions—IV. The control of magma properties and conduit geometry on eruption column behavior. Geophys. J. R. Astr. Soc., 89: 117-148.

Wohletz, K. H., 1983. Mechanisms of hydrovolcanic pyroclast formation: grain-size, scanning electron microscopy, and experimental results. J. Volcanol. Geotherm. Res., 17: 31-63.

Wohletz, K. H., 1994. How much do magmas degas during explosive eruptions ? A numerical approach. Geol. Soc. Amer. Abs. with Prog., 26(7): A451-A452.

Wohletz, K. H., Sheridan, M. F., and Brown, W. K., 1989. Particle size distributions and the sequential fragmentation/transport theory applied to volcanic ash. J. Geophys. Res., 94: 15,703-15,721.

Wolff, J. A., Wörner, G., and Blake, S., 1990. Gradients in physical parameters in zoned felsic magma bodies: implications for evolution and eruptive withdrawal. J. Volcanol. Geotherm. Res., 43: 37-55.

Wörner G., Harmon, R. S., and Hoefs, J, 1987. Stable isotope relations in an open magma system, Laacher See, Eifel (FRG). Cont. Mineral. and Petrol., 95: 343-349.

TABLES

Table 1. Average XRF Whole-Rock Pumice Analyses (Lower Member)

	LMat	LMt					
	LM-1	**LM-2**	**LM-3**	**LM-5**	**LM-9**	**LM-11**	**LM-13**
SiO_2	59.15	56.37	55.96	56.02	55.65	55.28	55.35
TiO_2	0.41	0.51	0.52	0.51	0.54	0.56	0.56
Al_2O_3	17.97	18.05	17.87	18.03	18.04	18.04	18.18
Fe_2O_3	0.42	0.67	0.75	0.73	0.76	0.80	0.81
FeO	2.75	4.46	4.96	4.88	5.11	5.27	5.31
MnO	0.14	0.13	0.12	0.12	0.12	0.13	0.13
MgO	0.47	1.27	1.29	1.29	1.39	1.59	1.62
CaO	2.28	3.96	4.11	4.08	4.26	4.48	4.60
Na_2O	4.34	3.55	3.52	3.52	3.36	3.39	3.44
K_2O	8.69	7.92	7.96	7.68	7.66	7.76	7.78
P_2O_5	0.08	0.24	0.29	0.25	0.27	0.29	0.29
Total	**96.70**	**97.13**	**97.35**	**97.11**	**97.16**	**97.59**	**98.07**
LOI*	3.42	2.95	2.71	2.96	2.89	2.48	1.94

* LOI assumed to be H_2O

Table 2. Average XRF Whole-Rock Pumice Analyses (Upper Member)

	UMat				UMt		
	UMa	**UMb**	**UMc**	**UMd**	**UMe**	**UMf**	**UMg**
SiO_2	58.10	58.36	57.90	58.20	57.16	55.92	54.35
TiO_2	0.43	0.42	0.42	0.41	0.42	0.50	0.61
Al_2O_3	17.78	17.90	17.78	17.76	17.70	17.86	18.09
Fe_2O_3	0.52	0.52	0.54	0.51	0.61	0.73	0.91
FeO	3.46	3.48	3.58	3.38	3.95	4.80	5.78
MnO	0.13	0.13	0.12	0.12	0.12	0.12	0.13
MgO	0.60	0.54	0.58	0.54	0.79	1.14	1.82
CaO	2.58	2.53	2.61	2.44	2.77	3.76	5.05
Na_2O	4.10	4.16	4.08	4.16	3.69	3.43	3.21
K_2O	8.51	8.42	8.34	8.45	8.85	8.63	8.07
P_2O_5	0.16	0.14	0.15	0.14	0.20	0.27	0.39
Total	**96.37**	**96.60**	**96.10**	**96.11**	**96.26**	**97.16**	**98.41**
LOI*	3.78	3.55	4.06	4.03	3.91	2.93	1.41

* LOI assumed to be H_2O

Table 3. Comparison of Blocky and Vesicular Shard Compositions*

	Vesicular		Blocky	
	LM-3	**LM-4**	**LM-3**	**LM-4**
SiO_2	57.34	56.79	62.98	61.93
TiO_2	1.02	0.97	0.65	0.69
Al_2O_3	15.79	16.21	15.86	15.68
FeO	6.97	7.17	4.49	5.20
MnO	0.25	0.32	0.23	0.22
MgO	0.48	0.48	0.09	0.19
CaO	5.86	5.59	3.26	3.51
Na_2O	0.91	1.00	0.84	0.86
K_2O	11.33	11.33	11.60	11.64
P_2O_5	0.00	0.14	0.00	0.00
H_2O	0.00	0.00	0.00	0.00
Total	**99.95**	**100.00**	**100.00**	**99.92**

* Averaged standardless energy dispersive spectral analyses: LM-3 vesicular (10 analyses); LM-4 vesicular (16 analyses); LM-3 blocky (11 analyses); and LM-4 blocky (10 analyses). Total Fe oxides shown as FeO; low values of Na_2O likely reflect Na loss under the electron beam.

FIGURES
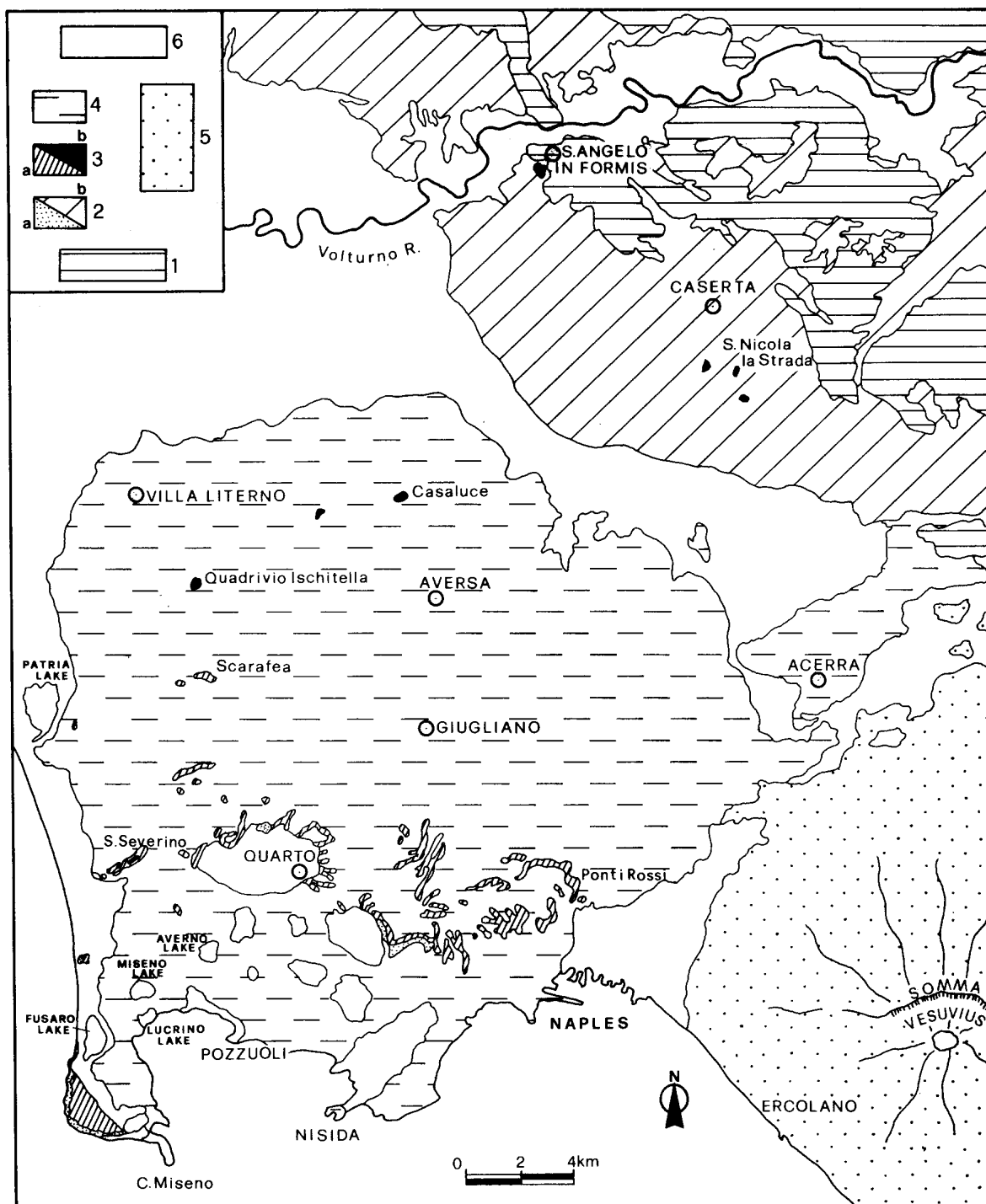
Fig. 1a   Geological sketch map of the Caserta Plain and surroundings modified from Orsi et al. (1991). Legend: (1) Rocks of the Apennines mountains, mostly limestones; (2a) volcanic rocks of the Phlegraean Fields older than the Campanian Ignimbrite; (2b) Campanian Ignimbrite; (3a) Upper and Lower Members of the Neapolitan Yellow Tuff; (3b) LM of the Neapolitan Yellow Tuff; (4) volcanic rocks of the Phlegraean Fields younger than the Neapolitan Yellow Tuff; (5) volcanic rocks of Somma Vesuvius; and (6) Recent and active sediments.
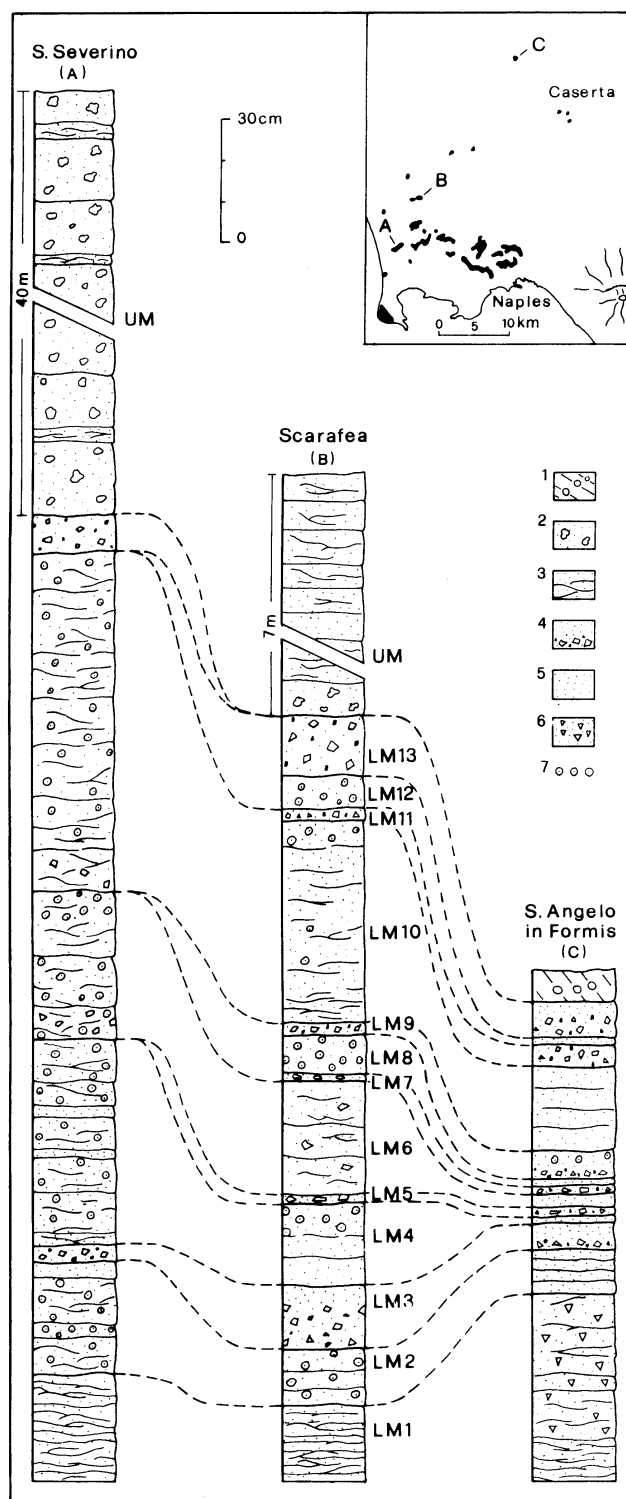
Fig. 1b   Stratigraphic sections (Orsi et al., 1992) representative of the proximal (San Severino), intermediate (Scarafea), and distal (Sant' Angelo in Formis) facies of the Neapolitan Yellow Tuff. Legend: (1) reworked deposits; (2) pyroclastic flow deposits; (3) pyroclastic surge deposits; (4) pumice-and-ash fallout deposits; (5) ash fallout deposits; (6) debris flow; and (7) accretionary lapilli..
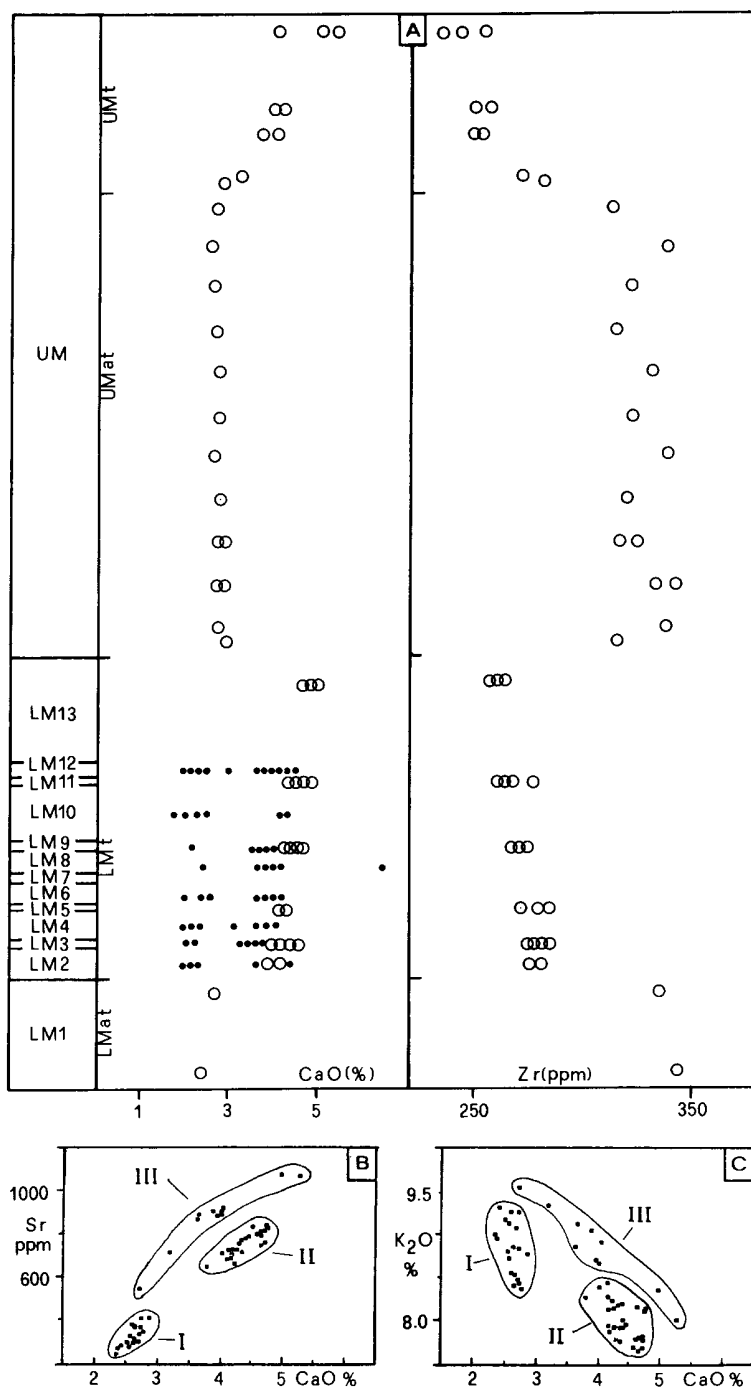
Fig. 2   (a) CaO and Zr content variations *vs* stratigraphic positions of the analyzed samples. Circles = XRF analyses of composite pumice samples; dots = microprobe analyses of glass shards and micropumices (Orsi et al., 1992). XRF whole-rock analyses of LM and UM pumices shown in Sr (b) and K_2O (c) *vs* CaO variation diagrams. Three magmas plot in distinct fields as alkali trachyte (I), trachyte (II), alkali trachyte to latite (III).
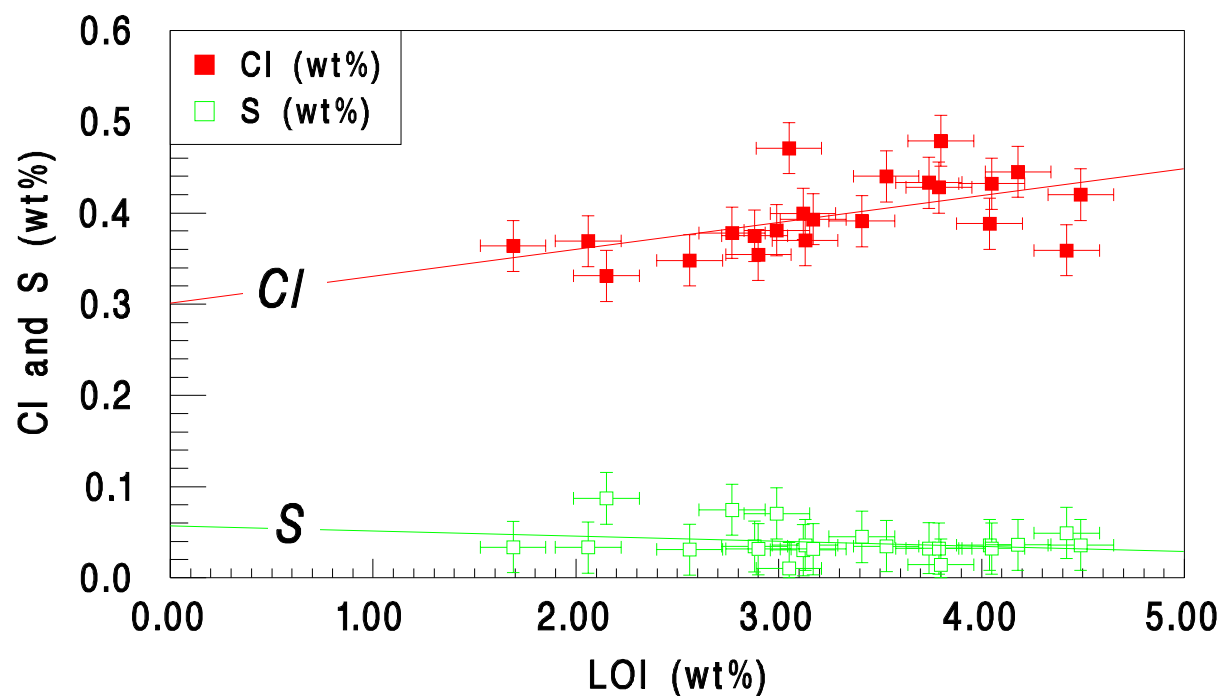
Fig. 3   Plot of Cl and S *vs* LOI for which the linear correlation of Cl = 0.029 (LOI) + 0.302 for the NYT trachytic tephra. This correlation is similar to that of Dunbar et al. (1989), who established a linear fit of Cl = 0.012 (H_2O) + 0.127 for rhyolitic Taupo tephra. The error bars represent ±0.15 wt% for LOI, ±0.03 wt% for Cl, and ±0.003 wt% for S (Cl and S analyses Roberto Santacroce, University of Pisa).
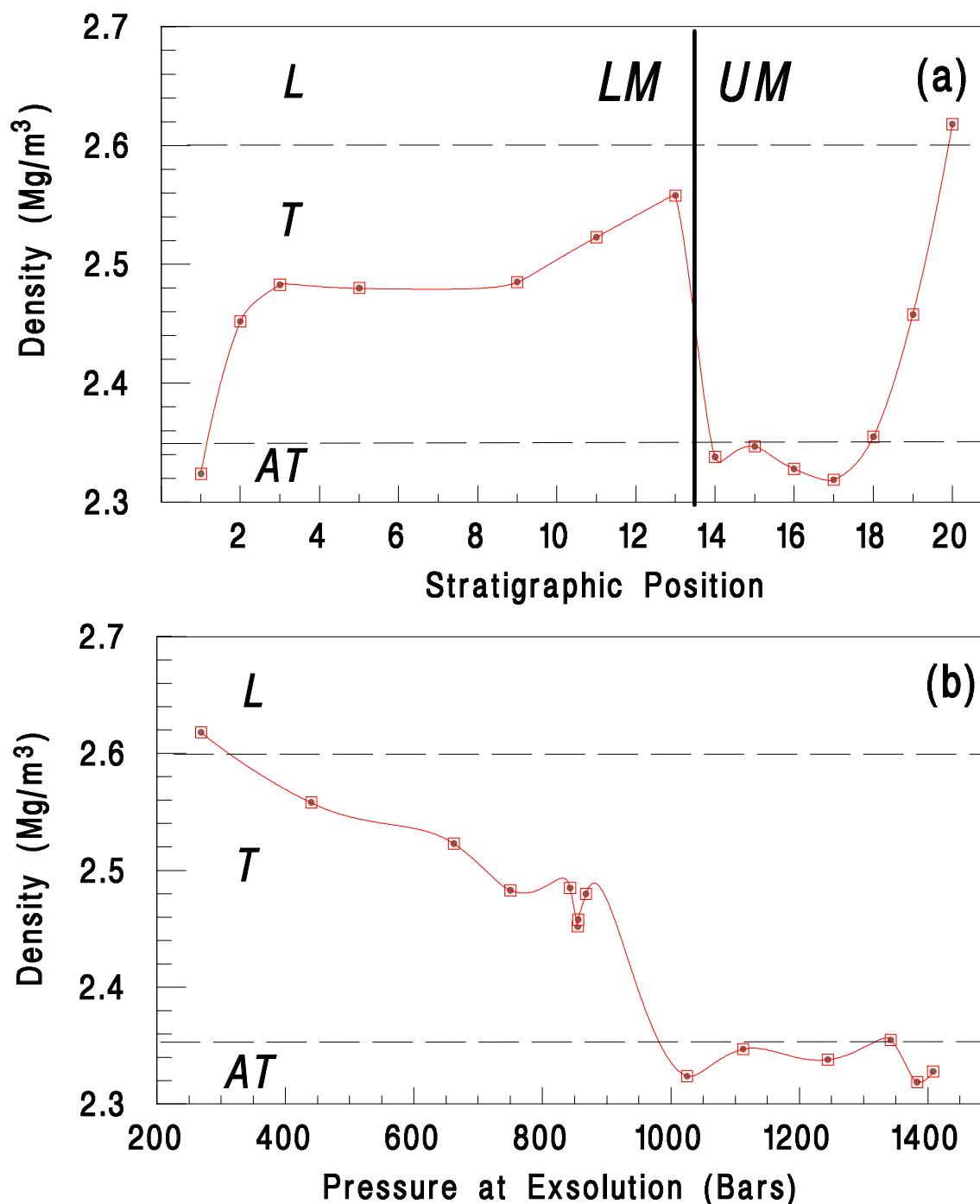
Fig. 4   (a) Maximum magma density plotted *vs* stratigraphic position. This density is that calculated at the pressure where all water is still in solution and vesicle nucleation is incipient. Sharp changes in density correlate to observed composition and textural variations observed for the 3 magmas: latite (L), trachyte (T), and alkali trachyte (AT). (b) Maximum density plotted *vs* pressure at exsolution where density is a function of magma composition and decreases with increasing pressure. This plot shows the alkali trachyte begins exsolution at greatest depth and trachyte and latite at higher magma chamber levels, respectively.
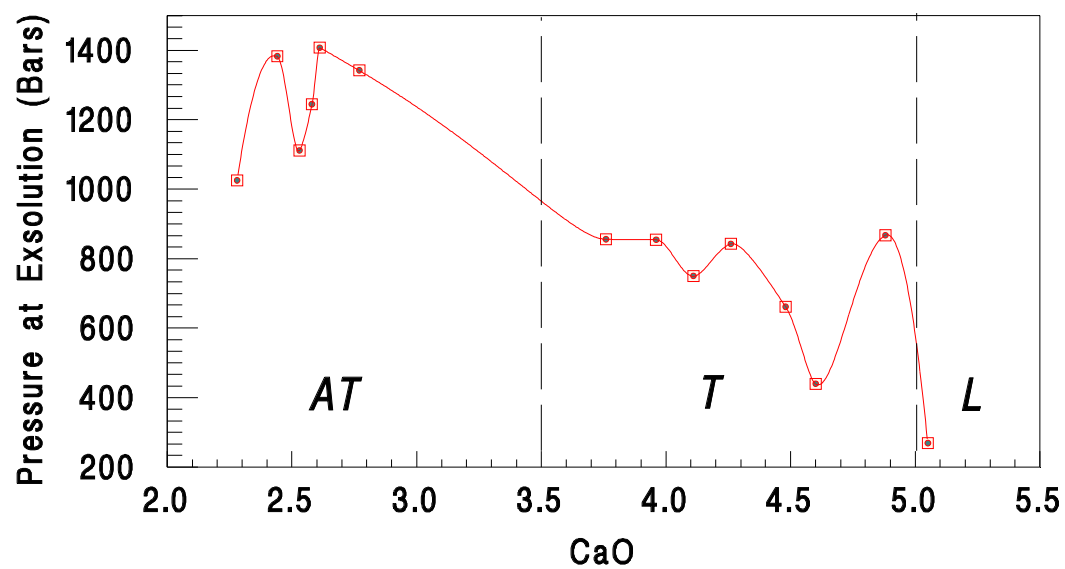
Fig. 5: Pressure at exsolution (incipient vesiculation) plotted *vs* CaO, showing vesiculation depth increases with magma evolution.
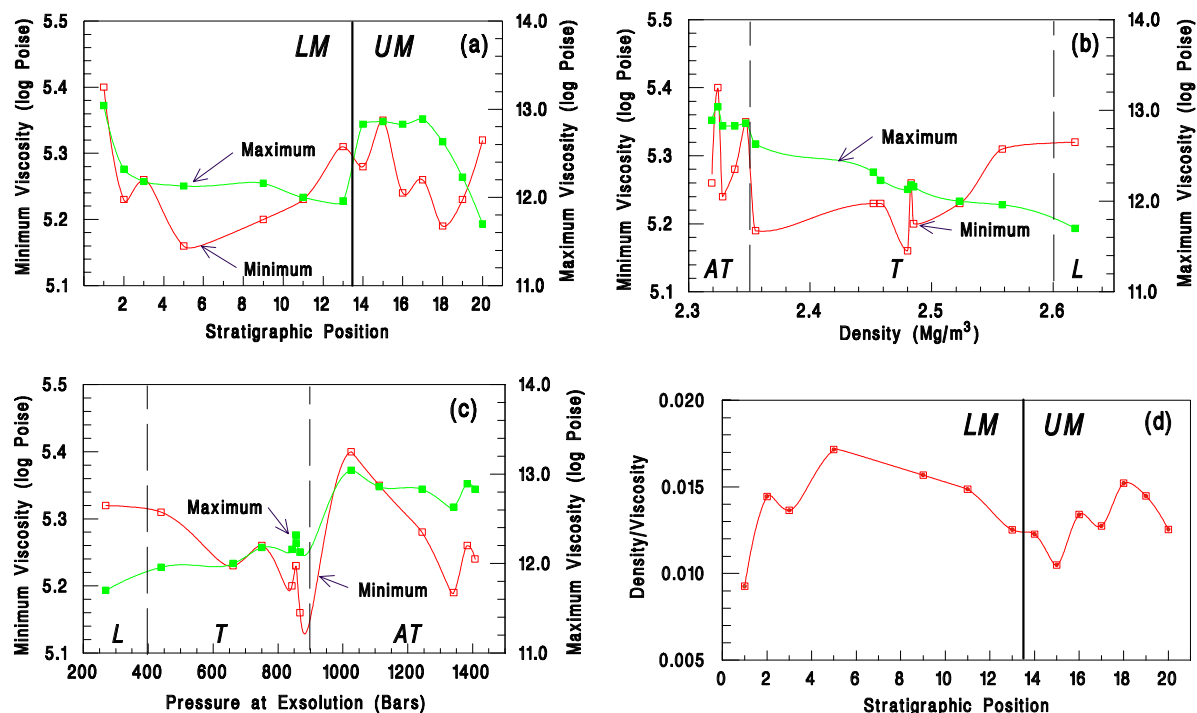
Fig. 6: Plots of viscosity dependence on sample stratigraphic position, sample density, and sample vesiculation pressure. (a) Maximum and minimum viscosities *vs* stratigraphy. In this plot, maximum viscosity is calculated at 1 bar pressure where most water has exsolved, and minimum viscosity is calculated for magma with all water in solution (high P). (b) Maximum and minimum viscosity *vs* maximum density shows alkali trachytes (AT) having higher viscosities than trachytes (T), and Latites (L) are intermediate. (c) Maximum and minimum viscosities *vs* pressure at exsolution. For each composition and magma batch, viscosity decreases with increasing exsolution pressure (analogous to Kushiro experiments at high P). (d) Plot of density/ viscosity *vs* stratigraphic position.
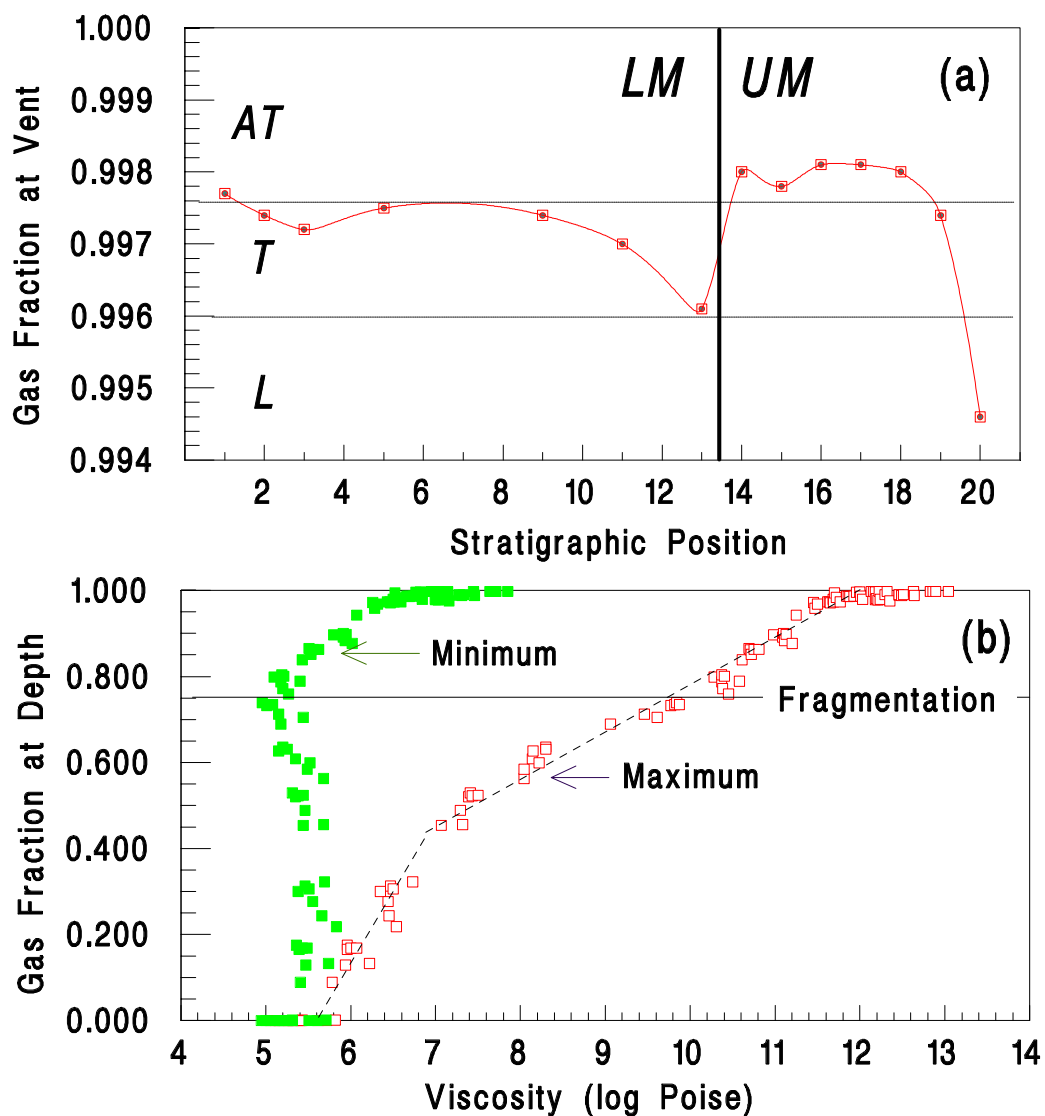
Fig. 7   (a) Gas volume fraction exsolved at 1 bar *vs* stratigraphic position shows an overall decrease in gas fraction with time during the eruption of LM and UM.   (b) Plot of gas fraction *vs* maximum viscosity shows higher gas contents associated with higher viscosity magmas. A break in slope for this relationship is shown for maximum viscosities near 10^7 Poise, which Sparks (1978) suggested a point where increasing viscosity and surface tension play important roles in limiting vesicle bubble growth.
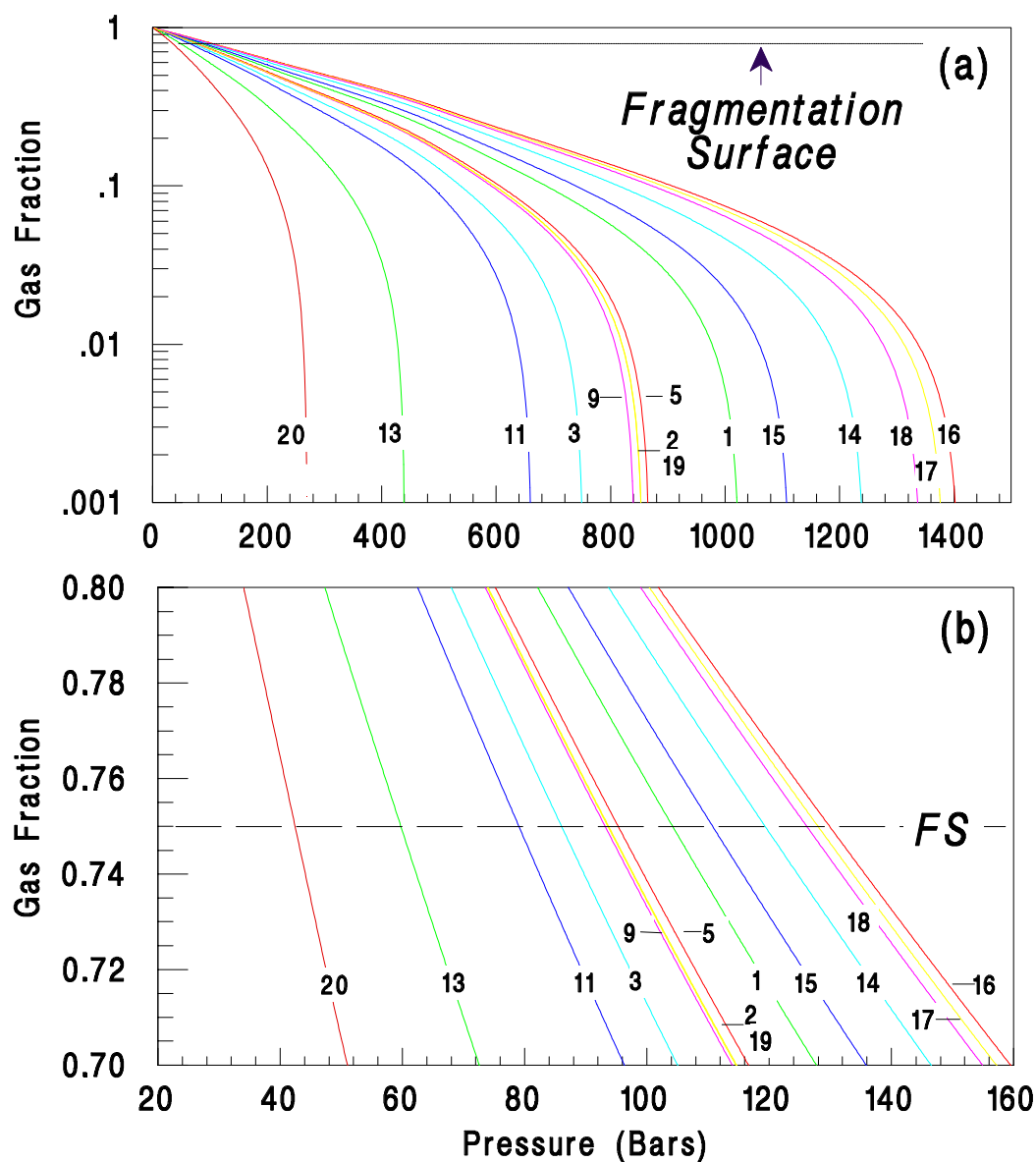
Fig. 8: (a) Gas volume fraction plotted with pressure inside the NYT magma chamber. This plot shows the increase in magma vesicularity as it rises to the top of the chamber where it becomes disrupted at the fragmentation surface (taken at a volume fraction of 0.75). By noting the curves for each sample, one can see the temporal variations in gas fraction displayed in Figure 6a. (b) Enlargement of the area near the fragmentation surface (FS).
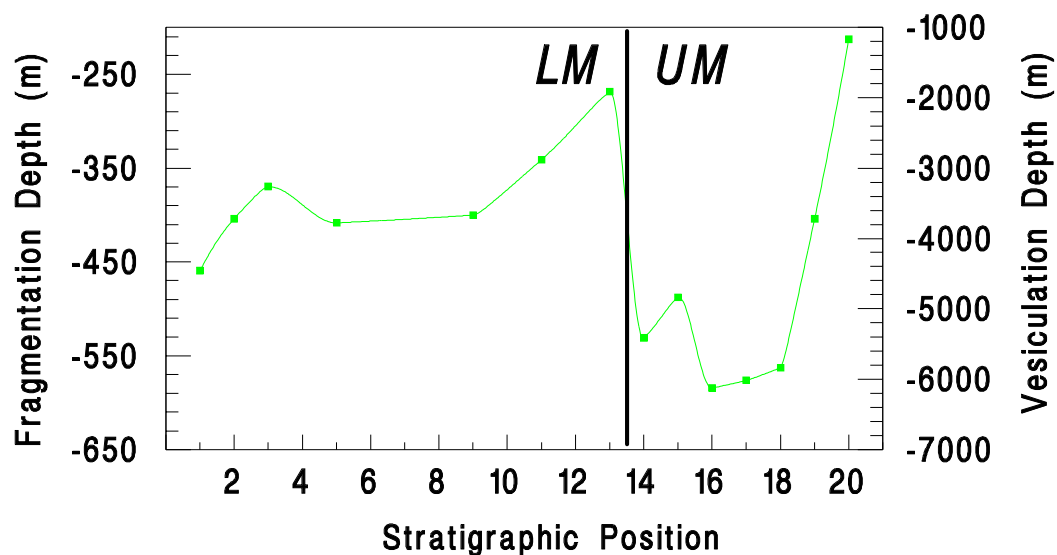
Fig. 9   The depth of the fragmentation and exsolution surfaces plotted as a function of stratigraphic position. During an eruption, the fragmentation surface theoretically migrates initially down conduit to a depth where its downward speed (localized multiphase sound speed) matches that of the magma rise. These plots show an general rise in the exsolution and fragmentation surface depths during the course of LM and UM eruptions that can be related to the general decrease of magma volatile content (Fig. 6) as well as magma rise rate.
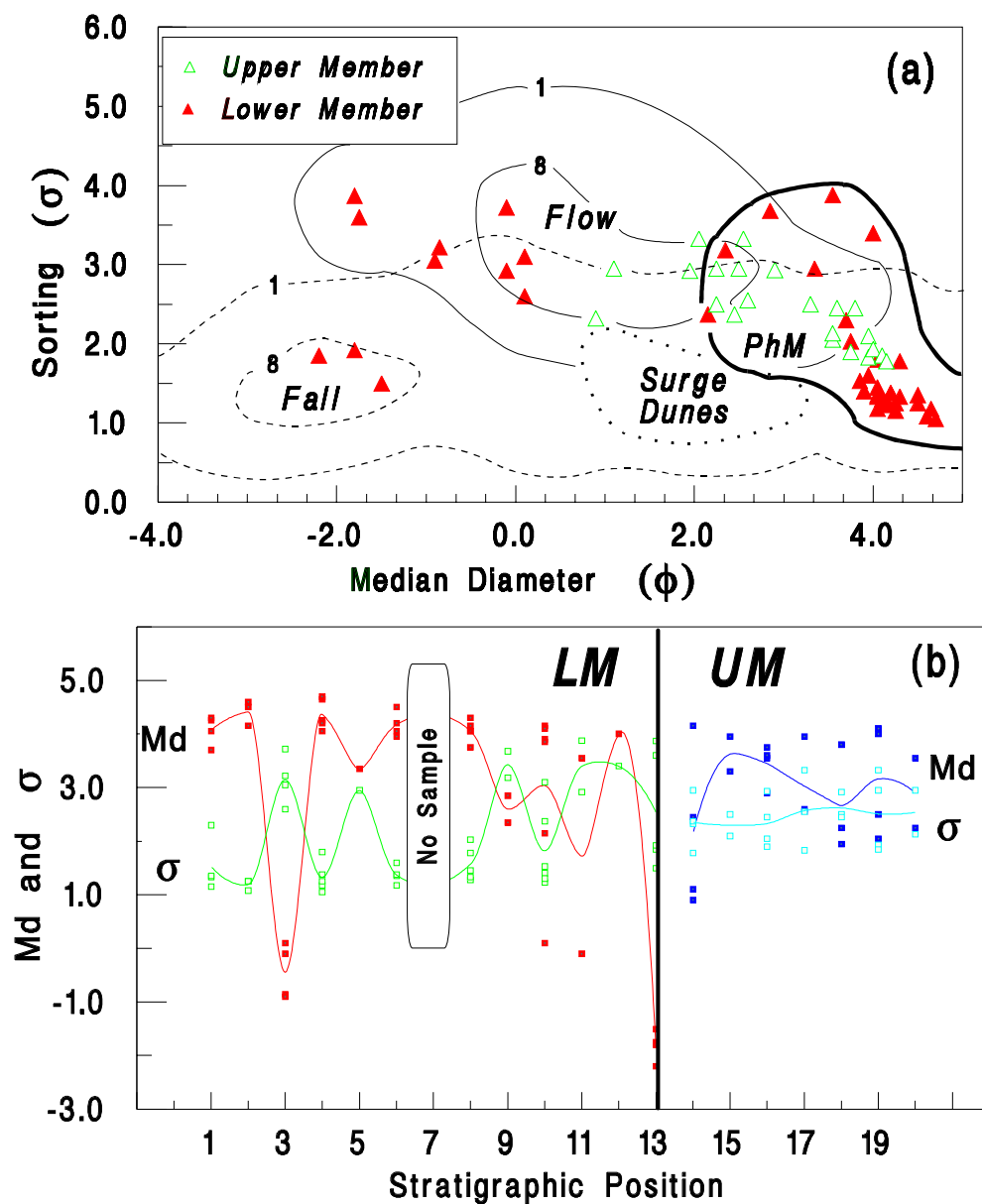
Fig. 10   Plots of sorting (σ) and median diameter (*Md*). (a) Walker diagram showing Walker's (1971) 1% and 8% fields of pyroclastic flows (enclosed by solid lines) and falls (enclosed by dashed lines) and that of pyroclastic surge dunes (enclosed by dotted line) (Fisher and Schmincke, 1984). A bold solid line encloses samples of a distinct phreatomagmatic character (PhM), the size and sorting characteristics of which are described by Sheridan and Wohletz (1983). (b) *Md* and σ *vs* stratigraphic position with curves passing through average values for each stratigraphic position. Note the opposite trends for these two parameters that show fallout units with coarser *Md* and better sorting than those of flows/surges.
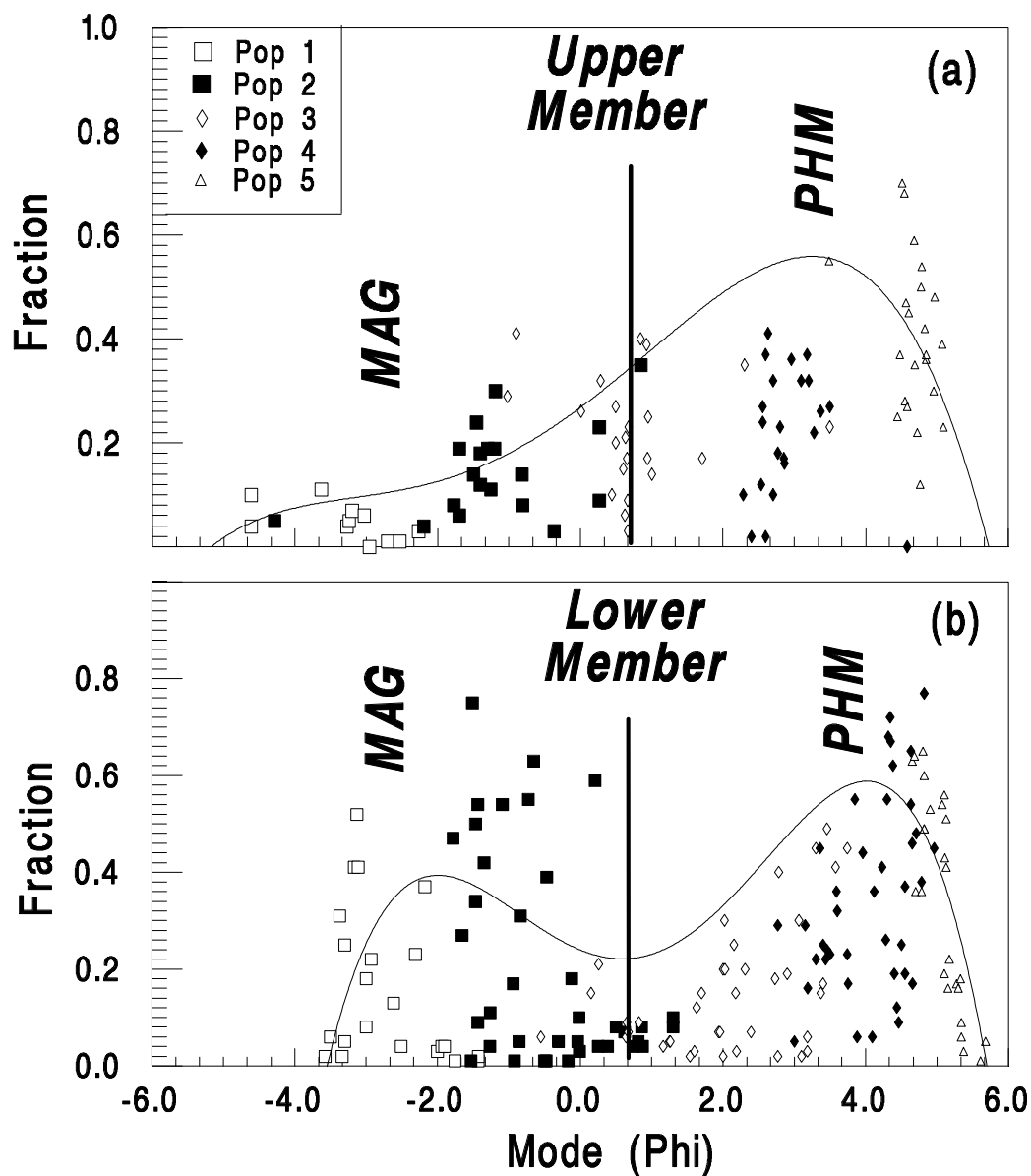
Fig. 11   Subpopulation fraction *vs* mode(ϕ_m) for upper (a) and lower (b) members, show approximate histogram averages for all samples. General trends, shown by polynomial curves, indicate two main groupings of subpopulations: coarse mode (subpopulations 1 and 2) are hypothetically assigned to magmatic fragmentation (MAG) whereas fine modes (subpopulations 3, 4, and 5) might be explained by hydrovolcanic (PHM) fragmentation. This distinction is best displayed in LM.
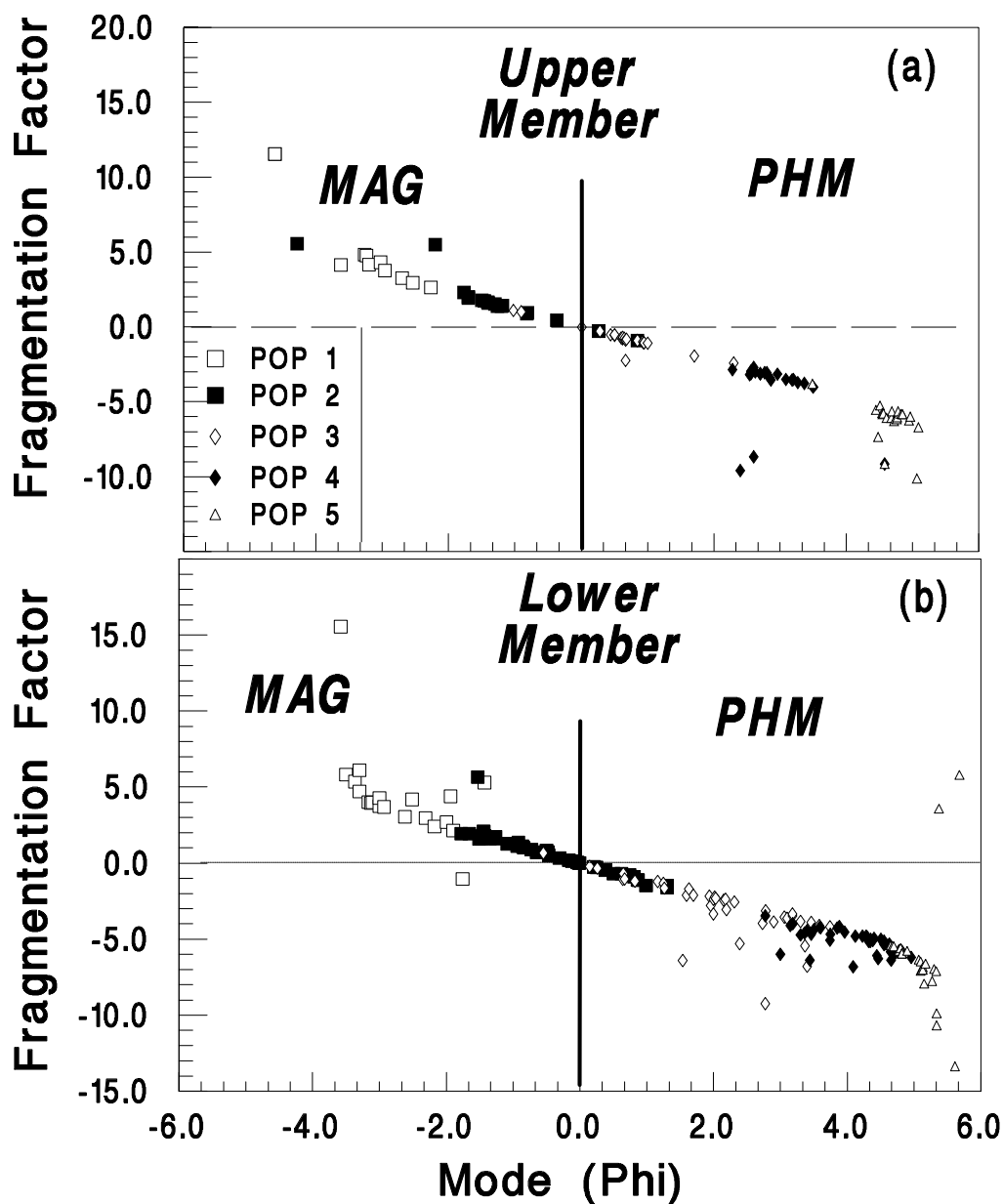
Fig. 12   Plots of the fragmentation factor (ϕ_m/γ) *vs* mode for the upper (a) and lower (b) members. These plots perhaps best distinguish magmatic and phreatomagmatic fragmentation characteristics, the former being coarser and less dispersed and the latter being fine and greatly dispersed (poorly sorted). In these plots the dividing line falls at 0.0 on both axes, which we believe is a general feature of pyroclastic and hydroclastic fragmentation.
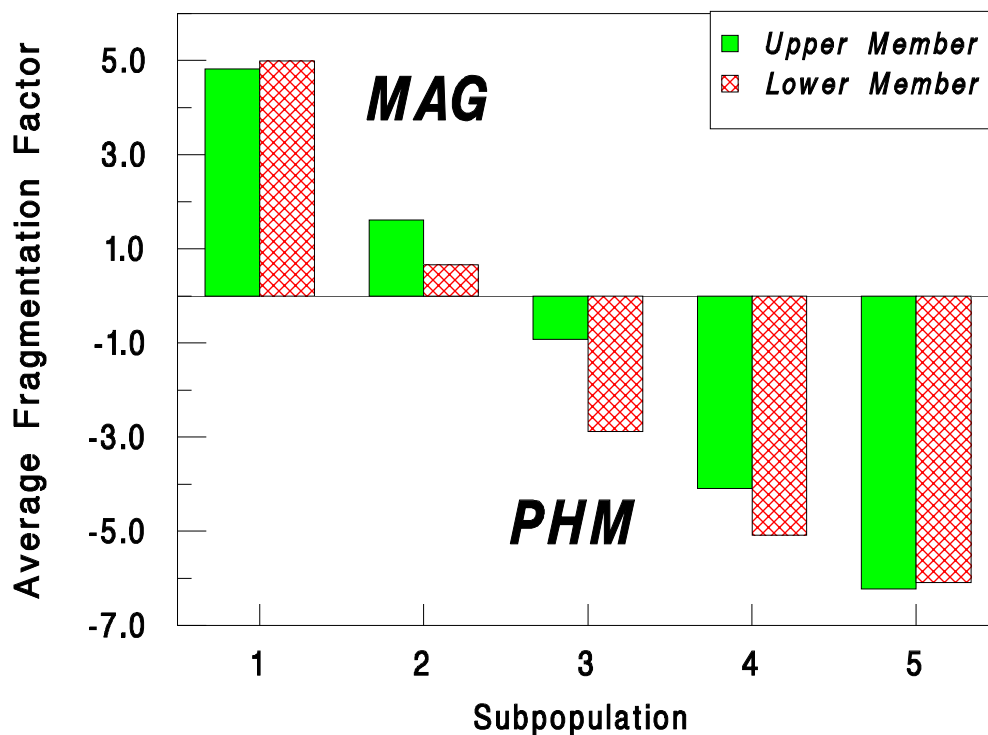
Fig. 13   In distinguishing magmatic and phreatomagmatic sample subpopulations, a histogram of average ϕ_m/γ values as a function of subpopulation shows that subpopulations 1 and 2 have a distinct character compared to that of subpopulations 3, 4, and 5, which allows us to designate the fragmentation mechanism that has produces these subpopulations.
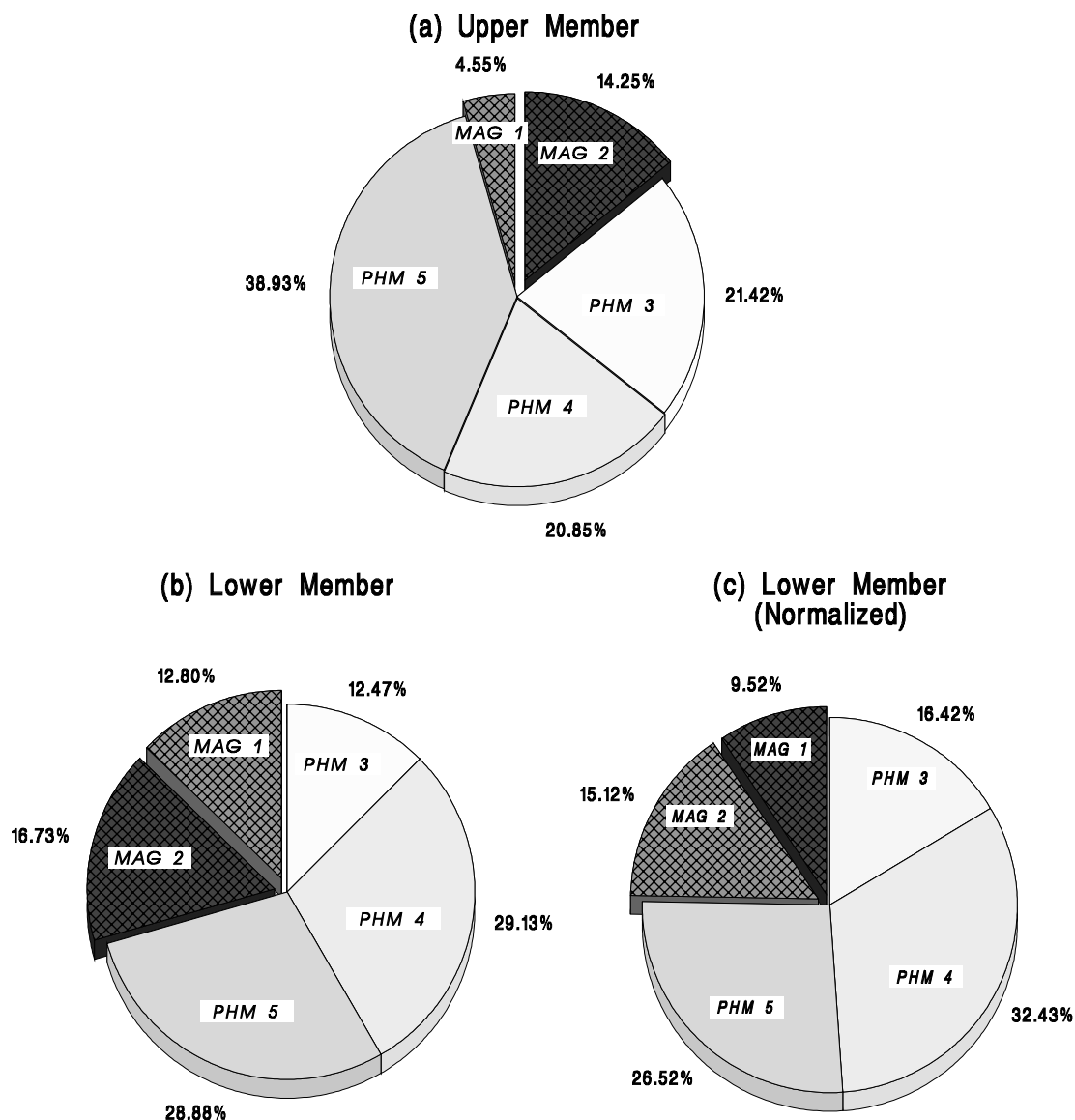
(a) Upper Member

4.55%

14.25%

MAG 1

MAG 2

38.93%   PHM 5

PHM 3   21.42%

PHM 4

20.85%

(b) Lower Member

12.80%

12.47%

MAG 1

PHM 3

16.73%

MAG 2

PHM 4   29.13%

PHM 5

28.88%

(c) Lower Member
(Normalized)

9.52%

16.42%

MAG 1

PHM 3

15.12%

MAG 2

PHM 4

PHM 5   32.43%

26.52%

Fig. 14   In comparing the average sample subpopulation fractions for the upper (a) and lower (b) members, pie diagrams show that about 80% and 70% of UM and LM samples, respectively, have phreatomagmatic origins. (c) For LM samples, subpopulation fractions are normalized by relative strata thickness, which indicates that by total deposit volume, about 75% of the tephra are phreatomagmatic.
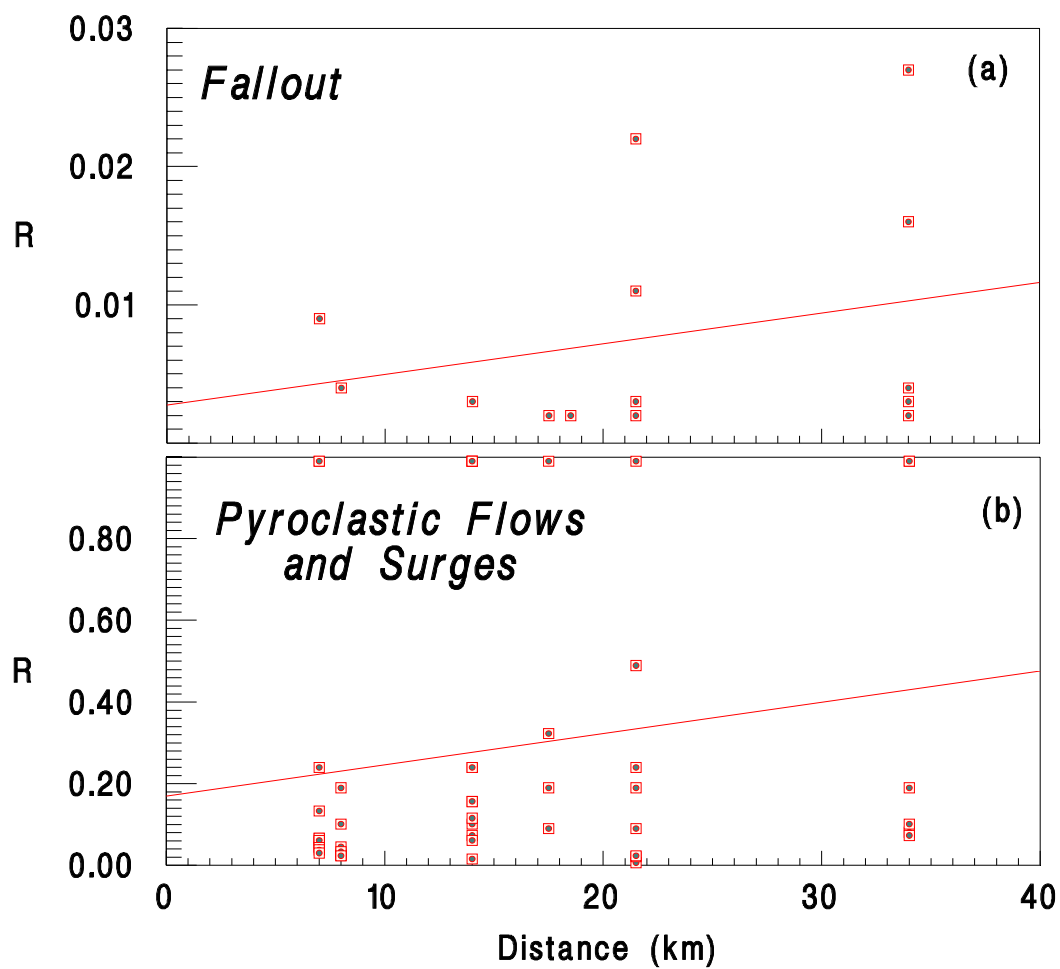
Fig. 15   Variation in calculated *R* (water/magma mass ratio) values with distance for fallout deposits (a) and pyroclastic flow and surge deposits (b). For the former *R* increases by 0.0002/km with distance while the latter shows an increase of *R* by 0.0095/km.
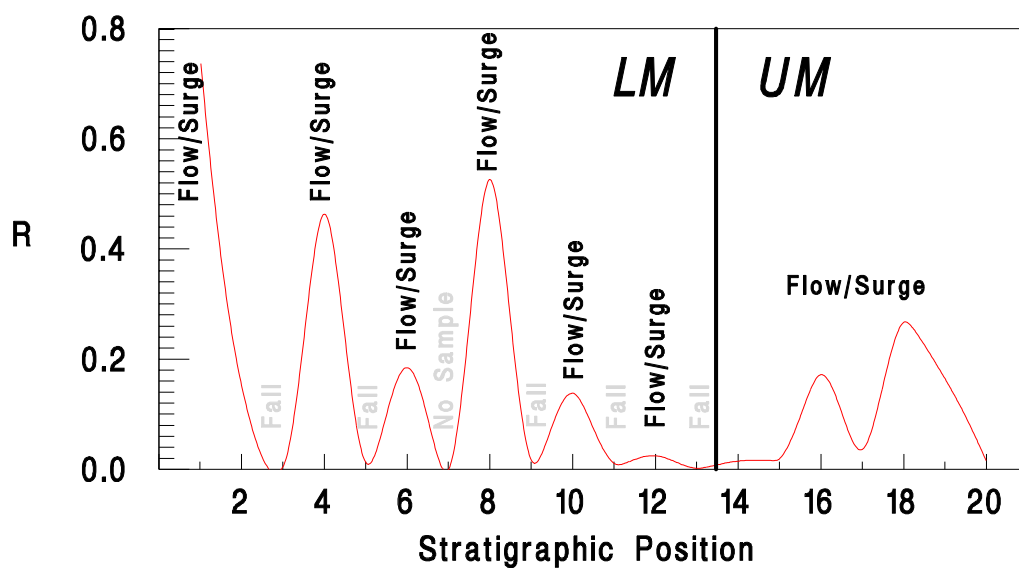
Fig. 16   In order to better display the trends of water/magma interaction for the NYT, average R values for ash and pumice layers were determined from Fig. 15. This plot of R vs stratigraphic position distinctly shows the higher water/magma interaction ($R = 0.15$ to 0.74) of LM than UM ($R = 0.02$ to 0.27).
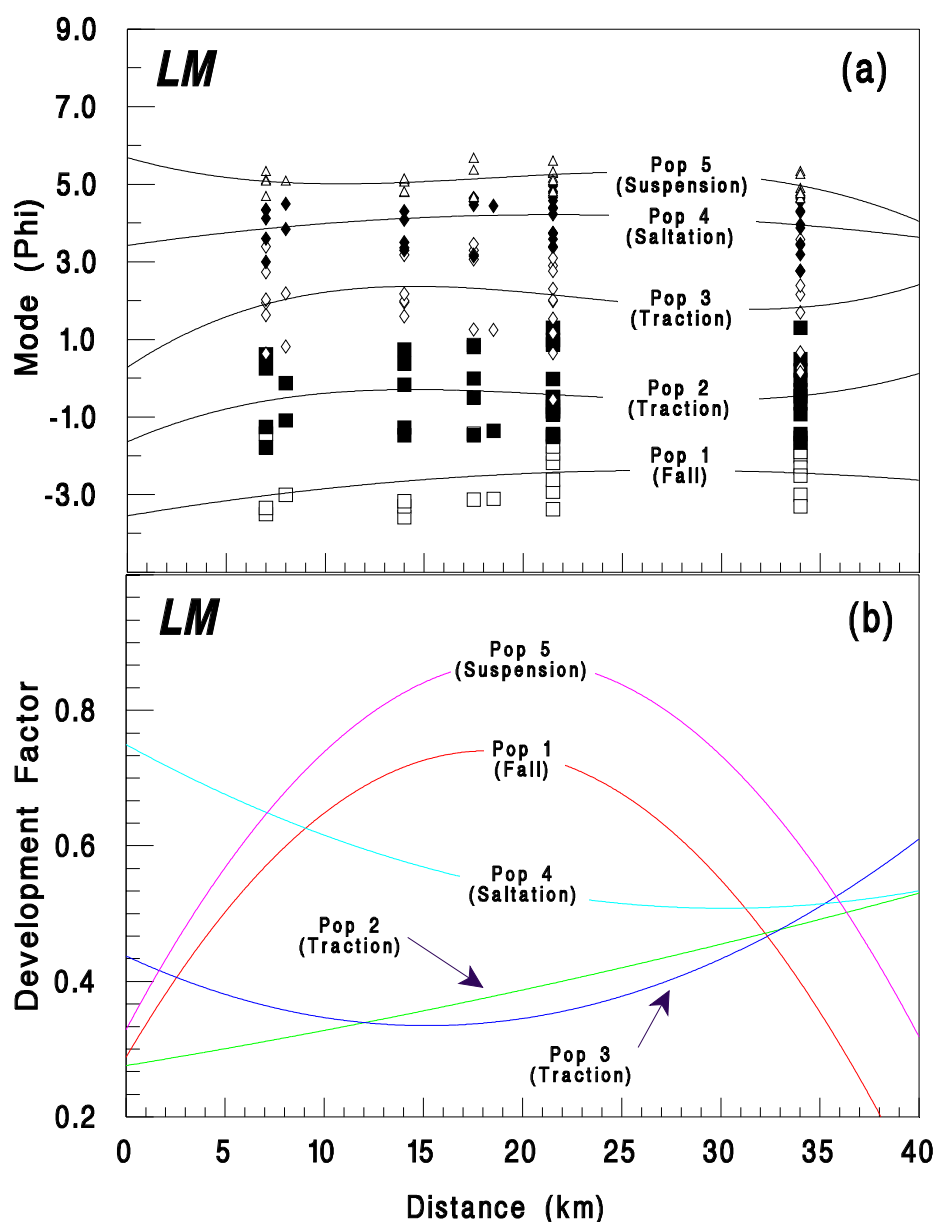
Fig. 17   (a) Average mode *vs* distance shows how subpopulation modes are fairly constant in grain diameter with distance. Assuming transport regimes based upon particle size (Wohletz et al., 1989), the following transport mechanisms are assigned to the 5 subpopulations. Subpopulation 1 (mode at about 8 mm) generally fines with distance and was likely transported by ballistic fallout. Subpopulations 2 and 3 show modes at about 0.25 and 0.75 mm respectively are fine enough to be carried along in ground hugging flows or surges but still coarse enough to be carried in a traction carpet. Subpopulation 4 with modes near 0.1 mm is fine enough to saltate at modest transport speeds, while subpopulation 5 (mode near 0.04 mm) is so fine that it likely stayed suspended during its transport. It shows a hint of coarsening with distance that may reflect its aggregation. (b) The degree to which each of these hypothetical transport mechanism may have developed is a function of their fraction and dispersion coefficient (sorting). This function, called the development factor $(1 + K + \gamma)$ is plotted with distance for each subpopulation. This plot of average development factor shows that traction carpet development (subpopulations 2 and 3) increases with distance, while saltation transport (subpopulation 4) decreases. Particle fallout (subpopulation 1) and suspended transport (subpopulation 5) are best developed at medial distances.
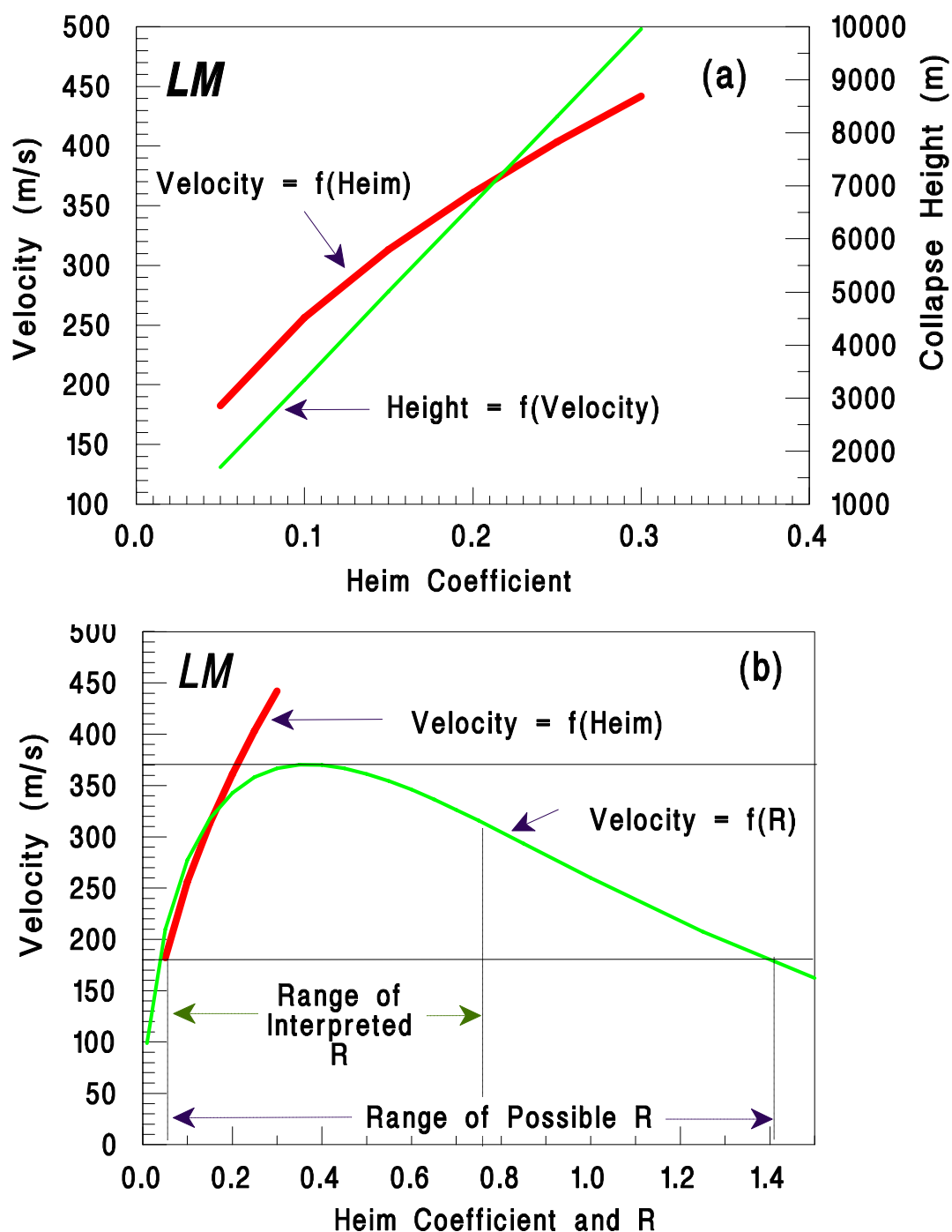
Fig. 18   (a) LM pyroclastic flow/surge velocities required to surmount preeruption topography and runout to a distance of 34 km as a function of Heim coefficient. Column collapse heights required to generate flow velocities are calculated as $(v^2/2g)$. This range of Heim coefficients predicts a range in velocity from about 200 to 450 m/s and column collapse height from 1500 to 10,000 m. (b) Eruptive column velocities as a function of R and Heim coefficient. The range of velocities calculated by Heim coefficient is compatible with a range of R from 0.05 to 1.4 and velocities between 170 and 370 m/s. Using the range of R interpreted from size data for the ash layers of LM ($0.2 < R < 0.65$), a restricted range of eruption column velocities between 320 to 370 m/s (near atmospheric sound speed) is predicted, fixing the Heim coefficient between 0.15 and 0.22 and column collapse heights between 5000 and 7000 m.
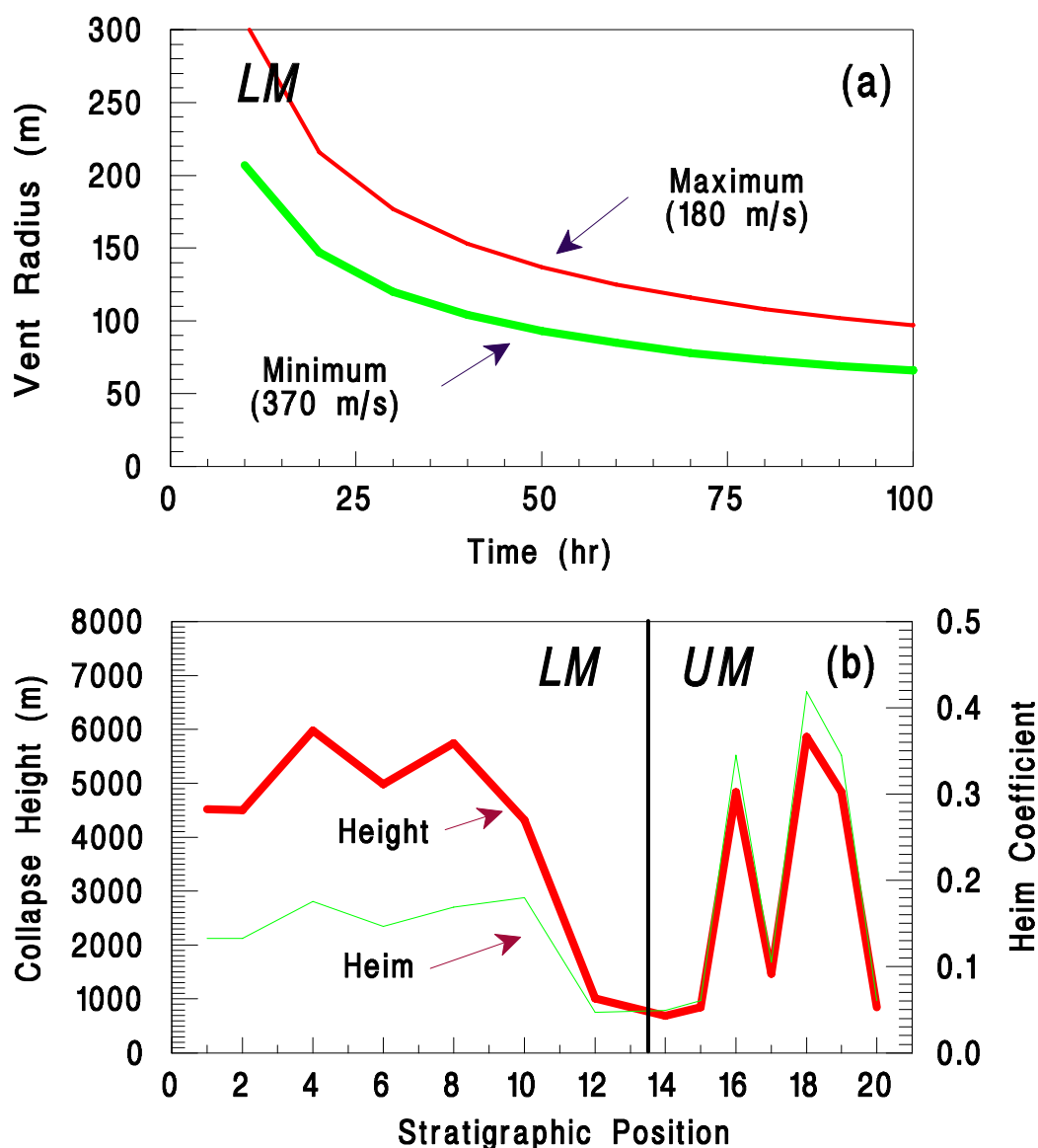
Fig. 19   (a) Calculated vent radii as a function of eruption duration for LM. Maximum and minimum values are calculated for the lower and upper range of column velocities, respectively shown in Figure 18. Vent radii in the range of 50 to 200 m are more likely values, considering the interpreted *R* values of the eruption. (b) Column collapse height and Heim coefficient *vs* stratigraphic position. LM shows generally higher column collapse heights than UM and a trend in Heim coefficient suggesting that the pyroclastic flows/surges became more mobile near the end of LM eruptions. For UM, a peak in eruptive column collapse height apparently occurred at intermediate times. Because the runout distance and preeruption topography for UM pyroclastic flows and surges is not known, the calculated Heim coefficient mimics that of collapse height: lower collapse heights require higher flow mobility (lower Heim).
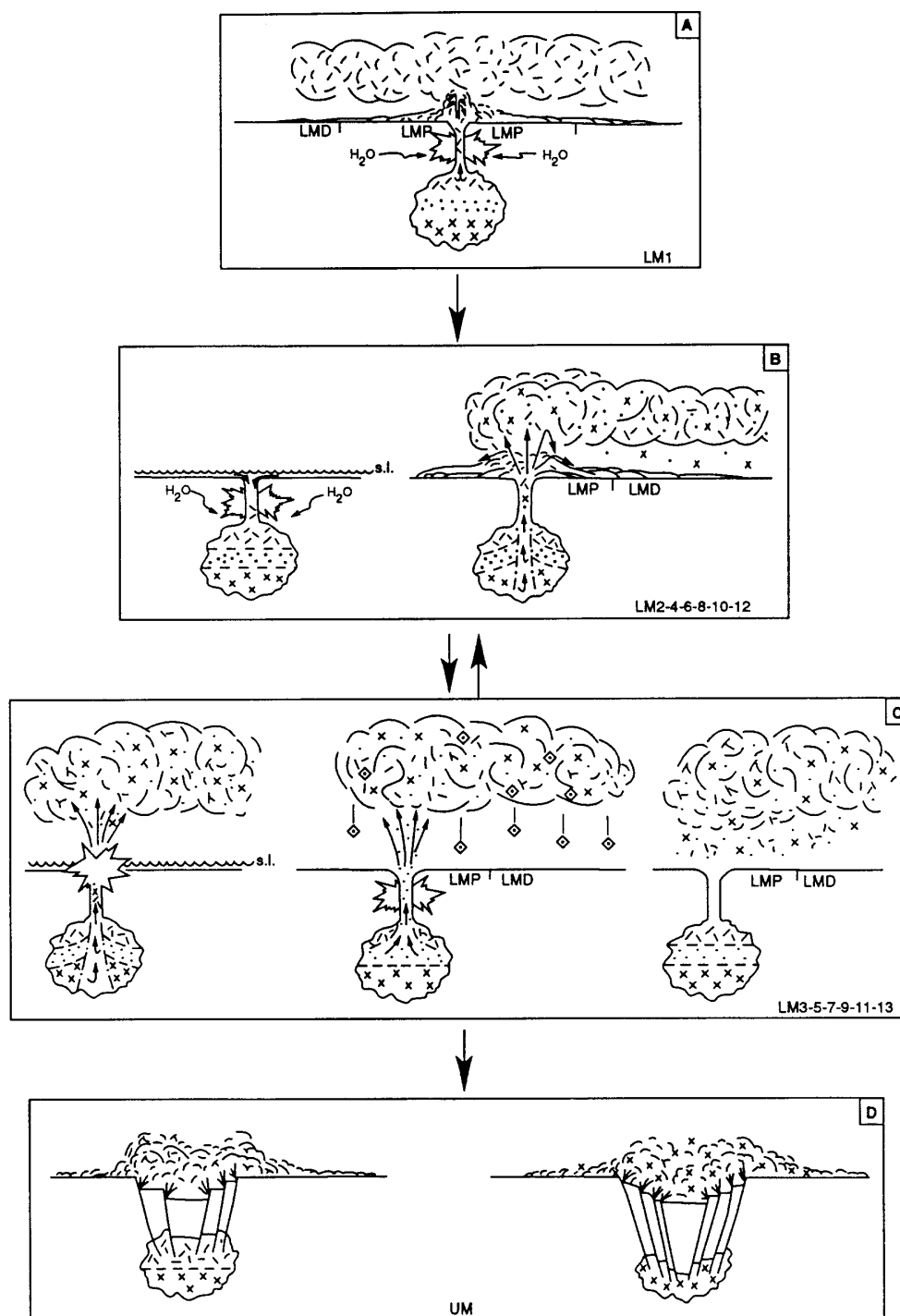
Fig. 20   Qualitative sketch illustrating magma chamber withdrawal and eruption column behavior during the
course of eruption of NYT LM and UM phases. For the magma chamber, three magma types are
denoted: alkali trachyte (dashes), trachyte (dots), and trachyte to latite (x). (a) Opening eruption of LM-
1 involved interaction of ground water and alkali trachyte (at magma chamber top) and produced
pyroclastic surges reaching distances of nearly 34 km from the vent. The following LM eruptions
alternated between phreatoplinian eruptions, marked by sea water pouring into the vent and commingling
of all three magma layers (b), and mostly Plinian eruptions where water interaction became limited during
the course of the eruption as did magma mixing during withdrawal (c). (d) UM eruptions occurred during
caldera collapse and tapped increasingly deeper levels of the chamber.